BILINGUAL PUBLISHING GROUP

Semiconductor Science and Information Devices

Volume 5 • Issue 1 • April 2023 ISSN 2661-3212(Online)

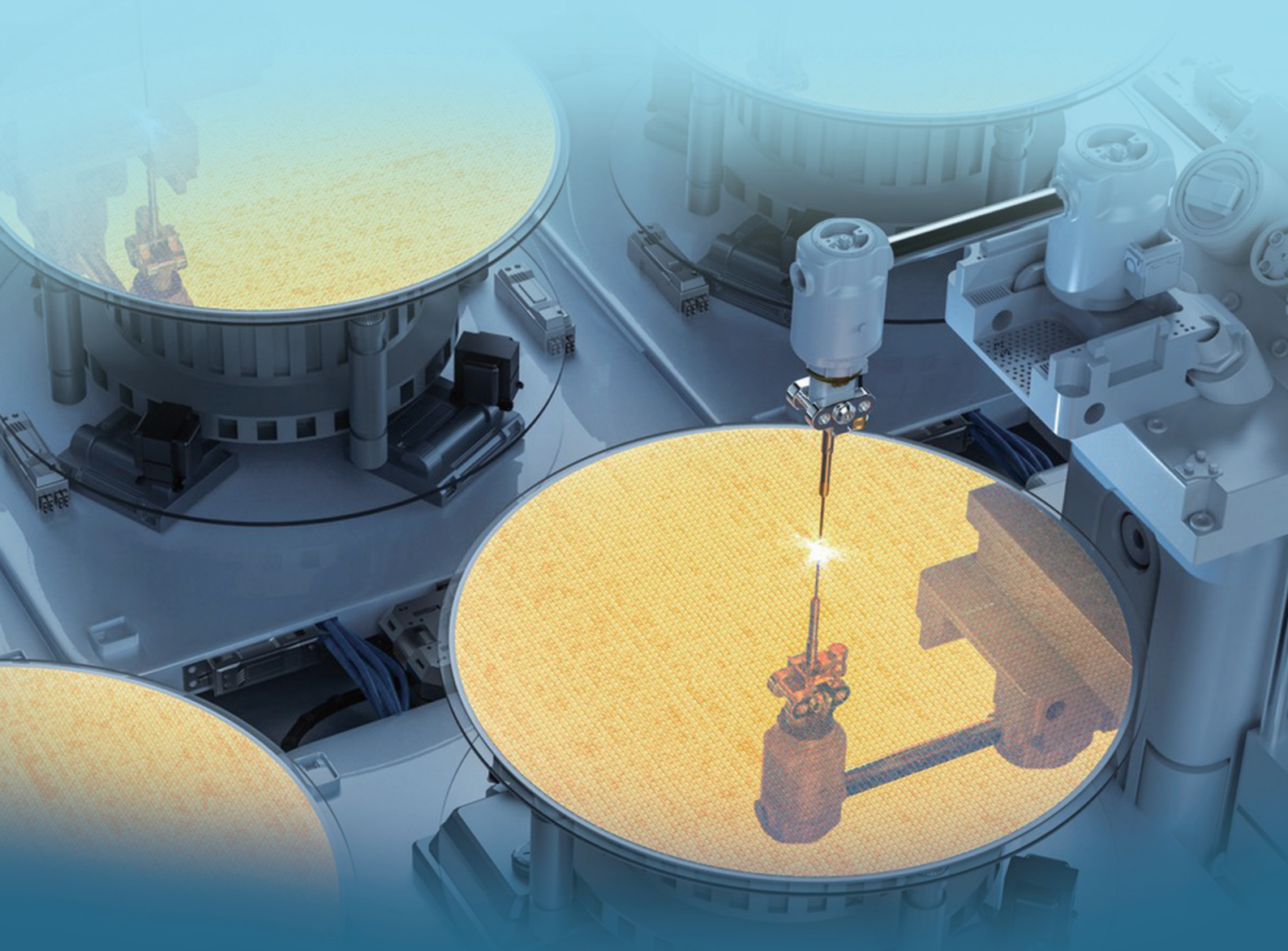

BILINGUAL PUBLISHING GROUP

Editor-in-Chief

Prof. Kasturi Vasudevan

Indian Institute of Technology Kanpur, India

Prof. Ahmed Saeed Hassanien

Benha University, Egypt

Editorial Board Members

Waqar Mahmood, Pakistan
Abbas Mohammed Selman, Iraq
Swayandipta Dey, Isreal
Hamed Dehdashti Jahromi, Iran
Chun-Hsiang Chang, USA
Shubhakar Kalya, Singapore
Muhammad Sana Ullah, USA
Suguo Huo, United Kingdom
Muhammad Azeem, U.A.E
Luka Strezoski, Serbia
Fikret Yildiz, Turkey
Yunyan Zhang, UK
Luca Persichetti, Italy
Vajeeston Ponniah, Norway
Thanikanti Sudhakar Babu, Malaysia
Muhammad Waqas Iqbal, Pakistan
Ren Li, Saudi Arabia
Prajoon Pavithran, India
Dongyan Zhang, China
Boualem Djezzar, Algeria
Jie Song, USA
Nihar R. Pradhan, USA
Feng Li, USA
Basanta Kumar Roul, India
Akram Sheikhi, Iran
Wenhui Yu, France
Elder Oroski, Brazil

Mahdi Bahadoran, Iran
Patrick Dela Corte Cerna, Philippines
Rahima Nasrin, Bangladesh
Husam Abduldaem Mohammed, Iraq
Niloufar Yavarishad, USA
Bikash Nakarmi, Nepal
Mebarka Daoudi, Algeria
Sergey Ivanovich Pokutnyi, Ukraine
Miao Zhou, China
Chunqing Wang, China
Riadul Islam, USA
Luca Potì, Italy
Amalia N. Miliou, Greece
Ahmed El Oualkadi, Morocco
Shuo Gao, China
Gennadiy Burlak, Mexico
Meysam Zareiee, Iran
Tseung-Yuen Tseng, Taiwan
Shi-Hai Dong, Mexico
Zheng Han, China
Subash T. D., India
Girma Yohannis Bade, Ethiopia
Francisco Bulnes, Mexico
Zhixin Cui, USA
Guiying Shen, China
Auttasit Tubtimtae, Thailand

Volume 5 Issue 1 • April 2023 • ISSN 2661-3212 (Online)

Semiconductor Science and Information Devices

Editor-in-Chief

Prof. Kasturi Vasudevan

Prof. Ahmed Saeed Hassanien

BILINGUAL PUBLISHING GROUP

BILINGUAL PUBLISHING GROUP

Volume 5 | Issue 1 | April 2023 | Page1-32

Semiconductor Science and Information Devices

Contents

Editorial

Articles

BILINGUAL PUBLISHING GROUP

Semiconductor Science and Information Devices

https://journals.bilpubgroup.com/index.php/ssid

EDITORIAL

Minus Infinity Plus Infinity

Kasturi Vasudevan

Department of EE IIT, Kanpur, 208016, India

Mankind has always been fascinated by nature and has striven to understand its functioning. What lies beyond the stars, what hides inside atoms, how to reach the stars, how to tap the vast energy inside the atoms, what is the correlation between space and time and how to exploit it—these are only a sample of the infinite questions to which we seek answers. In this editorial we explore some of the pressing issues that we are currently trying to address.

First and foremost is renewable energy. With the rapid depletion of fossil fuels, there is an urgent need to look for alternatives in the form of solar, wind, tidal waves, hydro, geothermal and biomass. The current efficiency of solar panels is 23%, wind turbines 40%, tidal turbines 80%, hydro 90%, geothermal 17% and biomass 45%. Space-based solar power is an active area of investigation. The energy generated may have to be stored in batteries with fast charging and high power (or energy) to weight ratio. New generation lithium-ion, lithium-sulphur and solid state are batteries of the future with applications in transportation e.g., electric vehicles (EVs). When EVs are around, can electric airborne vehicles (EAVs) be far behind? Small passenger EAVs are currently in the prototype stage. However, for large passenger EAV, the main bottleneck is batteries. Solar-powered aircraft also appear to be a feasible option.

Close on the heels of EVs and EAVs are autonomous vehicles (AVs), which brings us to the realm of artificial intelligence (AI) and machine learning (ML). AI and ML are based on neural networks that use mixed-signal processing, that is, analog and digital. Analog computers are faster and consume less power compared to their digital counterparts. However, analog computers are less reliable and less accurate compared to digital computers. For large neural networks, a mix of both analog and digital processors is required. AVs find application in space exploration and mining. An

*CORRESPONDING AUTHOR:
Kasturi Vasudevan, Department of EE IIT, Kanpur, 208016, India; Email: vasu@iitk.ac.in

ARTICLE INFO
Received:10 April 2023 | Accepted: 19 April 2023 | Published Online: 25 April 2023
DOI: https://doi.org/10.30564/ssid.v5i1.5644

CITATION
Vasudevan, K., 2023. Minus Infinity Plus Infinity. Semiconductor Science and Information Devices. 5(1): 1-2. DOI: https://doi.org/10.30564/ssid.v5i1.5644

COPYRIGHT
Copyright © 2023 by the author(s). Published by Bilingual Publishing Group. This is an open access article under the Creative Commons Attribution-NonCommercial 4.0 International (CC BY-NC 4.0) License. (https://creativecommons.org/licenses/by-nc/4.0/).

aircraft is also an AV, since it uses fly-by-wire and instrument landing systems (ILS). Talking of space brings us to the pertinent question—is mankind going to be a multi-planetary species? If yes, what is going to be our mode of transport for interplanetary or intergalactic travel? Is it a warp drive, ion thruster or antimatter rocket? How do we adapt to different types of planetary environments? Will space mining lead to the discovery of new elements? Will the Periodic Table be modified?

Turning our attention to the telecommunications sector, we find that there is a demand for higher data rates per user for applications like AVs, remote teaching, remote surgeries, video conferencing and so on. The 6th generation (6G) and beyond wireless standards could improve the data rates using spatial multiplexing by having multiple antennas at the mobile handset as well as the base station. Having multiple antennas in the mobile handset is feasible in mm-wave frequencies (30-300 GHz). The propagation characteristics of mm-wave could be improved using reconfigurable intelligent surfaces (RIS). Present-day telecommunications take place at the speed of light. Perhaps it may be possible to use principles of quantum entanglement to achieve instantaneous telecommunication over any distance. Quantum computers can solve certain class of problems that are infeasible with conventional digital computers. Quantum cryptography could be used to improve telecommunication security. Photonic qubits or quantum chips could be used to operate a quantum computer at room temperature instead of near absolute zero. Whatever the application, be it solar panels, batteries, mixed-signal processors, rocket engines, RIS or quantum chips—materials science in association with signal processing will play a major role in the advancement of technology. It is also apparent that research is usually multidisciplinary. A product is a culmination of many ideas.

That said, before mankind ventures on interplanetary or intergalactic sojourns, it is necessary to conserve the flora and fauna at home. In particular, the air and water need to be cleaned up. By cleaning up, we mean, not polluting them in the first place. Are we going to explore $[-\infty, +\infty]$ in time or $10^{-\infty}, 10^{+\infty}$ in space or both are anyone's guess. There are exciting times ahead—if there is a wish to know and do more.

BILINGUAL PUBLISHING GROUP

Semiconductor Science and Information Devices
https://journals.bilpubgroup.com/index.php/ssid

ARTICLE

Optimization of ITO/V_2O_5/Alq_3/TPBi/BPhen/LiF/Al Layers Configuration for OLED and Study of Its Optical and Electrical Characteristics

***Ritu*[1], *Sandhya Kattayat*[2], *H. K. Sublania*[3], *S. Z. Hashmi*[4], *Jasgurpreet Singh*[5], *P. A. Alvi*[1*]**

[1] *Department of Physical Science, Banasthali Vidyapith, Banasthali, Rajasthan, 304022, India*
[2] *Higher Colleges of Technology, PO Box-25026, Abu Dhabi, UAE*
[3] *Department of Physics, Government College, Bhadra, Hanumangarh, Rajasthan, 335501, India*
[4] *Department of Chemistry, Banasthali Vidyapith, Banasthali, Rajasthan, 304022, India*
[5] *University Centre for Research & Development, Department of Mechanical Engineering, Chandigarh University, Gharuan, Punjab, 140413, India*

ABSTRACT

Nowadays, OLEDs have shown aesthetic potential in smart cards, sensor displays, other electronic devices, sensitive medical devices and signal monitoring etc. due to their wide range of applications like low power consumption, high contrast ratio, speed highly electroluminescent, wide viewing angle and fast response time. In this paper, a highly efficient organic LED ITO/V_2O_5/Alq_3/TPBi/BPhen/LiF/Al with low turn-on voltage and high optically efficiency is presented including electrical and optical characteristics. The simulation of electrical characteristics like current versus applied voltage, current density versus applied voltage, recombination prefactor versus excess carrier density characteristics and optical characteristics like light flux versus current density, light flux versus applied voltage and optical efficiency versus applied voltage has been explained. The physical design, working principle and thickness of different layers along with the process of formation of singlet and triplet excitons are discussed in detail. Here double electron transport layer (ETL), cathode layers are used to enhance the electrical and optical efficiency of OLED. The operating voltage is found to be ~ 3.2 V for the ITO/V_2O_5/Alq_3/TPBi/BPhen/LiF/Al heterostructure based OLED. The designed organic LED has achieved the maximum optical efficiency at 3 V.

Keywords: OLED; Alq_3; BPhen; TPBi; I-V characteristics

*CORRESPONDING AUTHOR:
P. A. Alvi, Department of Physical Science, Banasthali Vidyapith, Banasthali, Rajasthan, 304022, India; Email: drpaalvi@gmail.com

ARTICLE INFO
Received: 18 September 2023 | Revised: 8 October 2023 | Accepted: 9 October 2023 | Published Online: 12 October 2023
DOI: https://doi.org/10.30564/ssid.v5i1.5977

CITATION
Ritu, Kattayat, S., Sublania, H.K., et al., 2023. Optimization of ITO/V_2O_5/Alq_3/TPBi/BPhen/LiF/Al Layers Configuration for OLED and Study of Its Optical and Electrical Characteristics. Semiconductor Science and Information Devices. 5(1): 3-10. DOI: https://doi.org/10.30564/ssid.v5i1.5977

COPYRIGHT
Copyright © 2023 by the author(s). Published by Bilingual Publishing Group. This is an open access article under the Creative Commons Attribution-NonCommercial 4.0 International (CC BY-NC 4.0) License. (https://creativecommons.org/licenses/by-nc/4.0/).

1. Introduction

Organic LED has attracted a lot of attention owing to its many advantages like flat display panels, ecological lighting sources, tuneability, flexibility, wide viewing angle and fast response time [1-4]. Researchers and scholars are making a great deal of effort to fabricate OLEDs that have good stability, picture quality, durability, low operating voltage and the materials used to design them are cheap and easily available [5,6]. Recently, OLED has been industrialized as indoor lighting, bio-sensors, digital camera and mobile phones. However, fabricating OLED with good electrical and optical characteristics to be used as lighting source and large display panel is still challenging [7].

Vanadium oxide (V_2O_5) is readily accessible, earth abundant and nontoxic. Vanadium oxide, a versatile substance that improves device performance, is essential in OLED technology. In OLEDs, it can be typically utilized as a hole transport layer (HTL). Without HTL there is carrier recombination on the surface of Alq_3 and bad ohmic contact between metal electrode and Alq_3. The influence of vanadium oxide (V_2O_5) as HTL on the performance of OLED has been investigated. For example, the operating voltage of OLED has been lowered by using vanadium oxide (V_2O_5). The effect of V_2O_5 on the device performance was investigated theoretically to provide complete future guidelines. For the eco-friendly, low cost vanadium oxide could be used as a good and promising candidate [8]. Vanadium oxide (V_2O_5) improves the exciton generation and suppresses the charge recombination [9]. It exhibits high charge carrier mobility and charge carrier transport capability. The work function of vanadium oxide is found to be comparable to that of Alq_3. The obstacle in the path of commercialization of OLED is the unavailability of ambient stable and efficient HTL material. Each layer present in OLED has its impact on the device's efficiency and power output. The HTLs and ETLs are critical for various reasons: (1) these are in direct contact with the emissive layer. (2) These layers are usually having thermal stability as compared to other layers in the heterostructure. (3) These layers play a pivotal role in increasing the charge transport properties.

There is a need of imminent research to design and develop highly reliable, long lasting and flexible lighting sources. In this paper, we focus on improving the efficiency of the device by using HTL (V_2O_5) and ETL (TPBi and Bphen) layers to provide better functionality and bypass the negative effects from OLED. Alq_3 (Tris(8-hydroxyquinolinato)aluminum) as an EML (emissive layer) has made a momentous contribution to improving optical efficiency and lowering its operating voltage. Alq_3 has been used as EML and ETL in the first commercial OLED produced by Tang. Alq_3 reacts immediately on coming in contact with the environment and water [10-12].

2. Structure configuration and working principle

OLED is a thin film optoelectronic device composed of organic semiconductors based on the principle of electroluminescence instead of LED technology composed of semiconductor material [13-15]. The organic semiconductors, in the form of semiconducting polymeric materials or organic molecules, are composed of hydrocarbon chain having properties like mechanical flexibility, highly efficient and highly feasible [16-22]. Initially, OLED consisted of single layer/monolayer and was less efficient because the injection of electrons and holes did not take place at the same time. Gradually double, triple and multi-layer OLEDs were developed to increase the efficiency [23]. Here, the four-layer OLED has been designed, as shown in **Figure 1**. The organic materials "BPhen and TPBi" has been used in ETLs; for EML purpose the organic material "Alq_3" has been utilized. For the purpose of HTL, a unique material V_2O_5 has been used. The HTL (V_2O_5) and ETL (TPBi/BPhen) play an important role in confining electrons and holes in active layers so that there is no quenching of excitons at the layer interface. All the layer specifications (materials along with their role and layer size) for the ITO/V_2O_5/Alq_3/TPBi/BPhen/LiF/Al heterostructure OLED have been illustrated in **Table 1**.

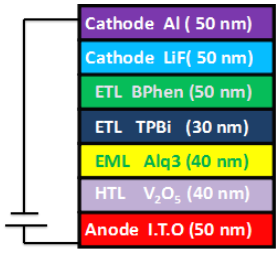

Figure 1. Layered structure of the ITO/V_2O_5/Alq_3/TPBi/BPhen/LiF/Al heterostructure OLED.

In this case, when a voltage is applied to oppositely charged electrodes i.e. anode and cathode, the electrons and holes are injected into the active layer from the cathode (LiF/Al) and anode (ITO), respectively. See **Figure 2**. The work function of adjacent layers is so low that there is ohmic contact between two different layers that can support the transportation of carriers. Hence, the transportation of carriers could take place readily without any barrier. The recombination of electrons and holes takes place in the emissive layer results the formation of singlet and triplet exciplex/excitons. The ratio in which singlet and triplet excitons are produced is 3:1 [24,25]. The emission of light takes place from the emissive layer and color of light or wavelength of light depends on the difference between the energy gap of the uppermost occupied molecular orbital (HOMO) and the lowest vacant molecular orbital (LUMO).

Table 1. Layers specification for the ITO/V_2O_5/Alq_3/TPBi/BPhen/LiF/Al OLED.

S. No.	Layer specifications	Thickness (nm)	Materials used
1	Anode	50	ITO (indium titanium oxide)
2	Cathode	50	Al (Aluminium)
3	Cathode	50	LiF (Lithium Fluoride)
4	HTL	40	Vanadium (V) oxide
5	EML	40	Alq_3 (tri-(8-hydroxyquinoline))
6	ETL	50	TPBi (2,2',2"-(1,3,5-Benzyinetriyl)-tris(1-phenyl-H-benzimidazole)
7	ETL	30	Bphen (Bathophenanthroline)

The brightness or luminescence of light depends on the amplitude of the voltage applied. It is very difficult to control the amount of charge carriers reach at the emissive layer; it should be equal in number so that recombination results in the emission of light. The mobility of holes is more than that of electrons inside the active layer [26,27]. ITO has high work function, good optical transparency, excellent hole injection properties, ease of patterning and high electrical conductivity. Further, ITO is a well-known n-type degenerate semiconductor with an optical band gap of 3.5-4.3 eV and has high transmission in the near infrared and visible regions of the electromagnetic spectrum [28]. These properties of ITO influence the optical and electrical characteristics of OLED [29]. LiF plays a crucial role in improving OLED durability and efficiency. It has been used widely to modify chemical reactivity at interface, electrode work function and contact adhesion [30-36]. It can be kept on the top as well as the bottom of the device as the electrodes as well as the substrate. The energy band diagram of the design with the layer specifications ITO/V_2O_5/Alq_3/TPBi/BPhen/LiF/Al OLED has been illustrated in **Figure 2**.

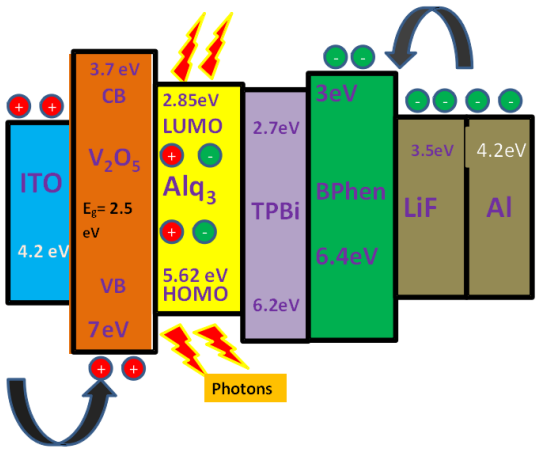

Figure 2. Layer specification in ITO/V_2O_5/Alq_3/TPBi/BPhen/LiF/Al OLED.

3. Simulation results and discussion

Understanding OLEDs' electrical behaviour and efficiency requires an understanding of their I-V (current-voltage) properties. These qualities aid engineers in fine-tuning OLED devices, guaranteeing effective control over power usage and brightness. Studying I-V curves also helps with problem-solving and diagnosis, which enhances the performance and

lifespan of OLED displays.

To calculate the value of the potential profile i.e. φ Poisson Equation (1) has been used. Further, to study the motion of free electrons and holes within the OLED of ITO/V_2O_5/Alq_3/TPBi/LiF/Al, both electron and hole drift diffusion Equations (2) and (3) are used. Carrier continuity Equations (4) and (5) are solved to calculate the recombination and generation rate of electrons and holes inside the device [37-40].

$$\frac{d}{dx}\epsilon_0\epsilon_r\frac{\partial\varphi}{\partial x} = q(n-p) \quad (1)$$

$$J_n = q\mu_c n\frac{\partial E_c}{\partial x} + qD_n\frac{\partial n}{\partial x} \quad (2)$$

$$J_p = q\mu_n p\frac{\partial E_p}{\partial x} - qD_p\frac{\partial p}{\partial x} \quad (3)$$

$$\frac{\partial J_n}{\partial x} = q(R_n - G + \frac{\partial n}{\partial x}) \quad (4)$$

$$\frac{\partial J_p}{\partial x} = -q(R_p - G + \frac{\partial p}{\partial x}) \quad (5)$$

where, the terms used in Equations (1)-(5) have been explained as follows:

ϵ_0 = Electrical permittivity of free medium
μ_n = hole mobility
ϵ_r = Relative electrical permittivity
E_c = free electron mobility edge
φ = Voltage profile
E_p = free hole mobility edge
q = elementary charge on an electron
D_n = electron diffusion coefficient
n = free electron concentration
D_p = hole diffusion coefficient
p = free hole generation rate
R_n = electron recombination rate
J_n = electron current flux density
R_p = hole recombination rate
J_p = hole current flux density
G = free carrier generation rate
μ_c = electron mobility

With the help of simulation, we have determined the I-V characteristics of the designed OLED. **Figure 3** shows the current versus voltage characteristics of ITO/V_2O_5/Alq_3/TPBi/BPhen/LiF/Al-based heterostructure OLED. There is no variation in current with the increase in applied voltage till ~3.5 V. Further increase in bias voltage results in an exponential increase of current. On increasing the biased voltage applied between ITO and LiF/Al, there is an increase in the concentration of carriers, which are transported to the emissive layer with the help of TPBi/BPhen (ETL) and V_2O_5 (HTL). The recombination of electron and holes takes place in the emissive layer i.e. Alq_3 which result in the formation of exciplexes. There is the emission of light from the emissive layer. The upsurge of exciplexes results in an increment in the outflow of light. The turn-on voltage of the diode also depends on the energy gap between LUMO and HOMO of the emissive layer [41]. **Figure 4** shows the J-V characteristics of the designed heterostructure OLED. From 0 to 3.25 V, there is a minimal increase in current density with the applied biased voltage which is similar to that of a resistive diode. One can see from the graph that increasing the voltage after 3.2 V results in an exponential increase of current density. The obtained results for J-V characteristics completely agree with the I-V characteristics result. The efficiency of OLED estimated by most of the special technology and scientific interest is calculated from the luminescence/light flux multiplied by a factor of π, rather than from a value of light flux only [42]. Light flux is defined as the amount of light emitted per unit cross section area of the device [43]. There is a non-linear relationship between light flux and applied voltage in the low voltage region, it increases superlinearly from 2.5 V to 3.5 V and further increases i.e. above the operating voltage resulting in an exponential increase of light flux with the applied voltage. See **Figure 5**.

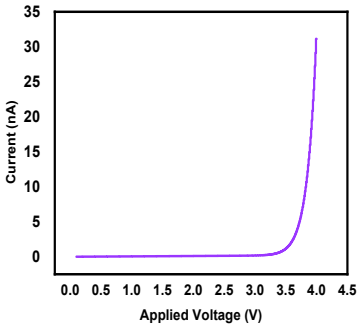

Figure 3. Current-voltage (I-V) characteristics of ITO/V_2O_5/Alq_3/TPBi/BPhen/LiF/Al OLED.

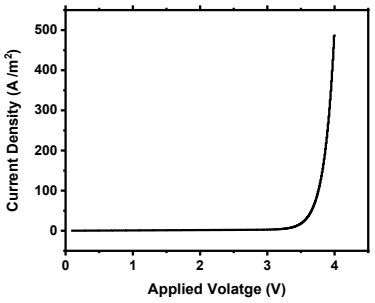

Figure 4. Current density-voltage (J-V) characteristics of ITO/V_2O_5/Alq_3/TPBi/BPhen/LiF/Al OLED.

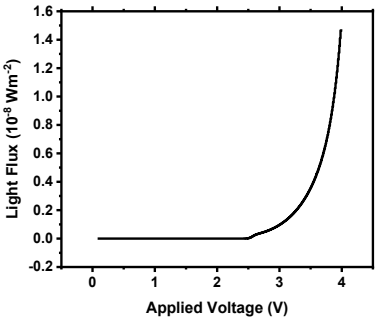

Figure 5. Plot of light flux vs applied voltage for ITO/V_2O_5/Alq_3/TPBi/BPhen/LiF/Al OLED.

Refer to **Figure 6**, which shows the plot of light flux Vs current density for the designed OLED. The light flux increases linearly after 75 A/m^2 value of current density. It means that the light radiated per unit area per unit time from the device increases with the increase in the current applied between the oppositely charged electrodes. The optical efficiency is defined as the amount of light radiated by OLED to the amount of voltage applied to device for this irradiance. For the designed organic LED, the peak value of optical efficiency is found to be at an applied voltage of 3.25 V which is very low. It means that organic LED starts to operate/glow at such a low voltage. At this voltage, maximum numbers of excitons i.e. electron and hole pairs bounded by coulombic forces of attraction are converted into photons. See **Figure 7**.

The recombination prefactor of the ITO/V_2O_5/Alq_3/TPBi/LiF/Al OLED has also been thoroughly studied. Bimolecular recombination is a fundamental phenomenon that controls how much light is generated, which has an impact on the effectiveness of organic optoelectronic devices like OLEDs. The recombination prefactor indicates the rate at which electron and holes are recombining to emit light. To determine the quantities (such as the generation of light and efficiency), the recombination prefactor is necessary. As shown in **Figure 8**, with the increase in excess charge carrier density, there is an exponential increase in the value of the recombination prefactor. Refer to **Figure 8**, up to 1.0×10^{22} excess carrier density, no recombination prefactor occurs, because such amount of excess carriers is not enough to produce the recombination. The probability of recombination increases with the increase in the carrier concentration of electrons and holes beyond the 1.0×10^{22} excess carrier density.

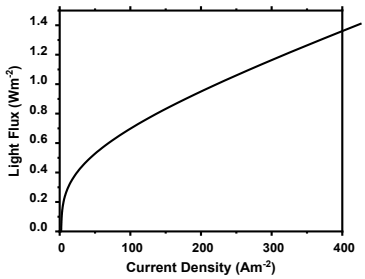

Figure 6. Plot of light flux vs current density for ITO/V_2O_5/Alq_3/TPBi/BPhen/LiF/Al OLED.

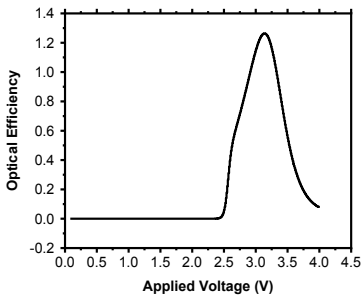

Figure 7. Plot of optical efficiency Vs applied voltage.

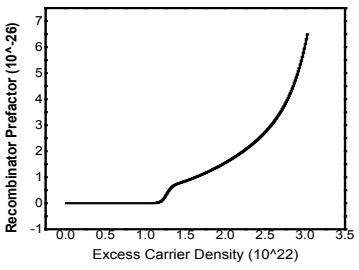

Figure 8. Plot of recombination prefactor Vs excess carrier density.

4. Conclusions

The structure optimization, as well as the optical and electrical properties of the ITO/V_2O_5/Alq_3/TPBi/LiF/Al OLED, has been studied using Poisson, bipolar drift diffusion and continuity equations. The operating voltage was found to be to be approx. 3.2 V. The optical efficiency of the device has been achieved to be optimum at 3.2 V. Definitely, the work reported will be an input for lowering the operation power and boosting the stability of OLEDs which are most weakest points of OLEDs for practical applications.

Author Contributions

All authors contributed to the study conception and design. Data generation, collection and analysis were performed by [Ritu], and [P. A. Alvi]. The first draft of the manuscript was written by [Ritu], [P. A. Alvi], [S. Z. Hashmi], [Jasgurpreet Singh] and [Sandhya Kattayt], commented on previous versions of the manuscript. All authors read and approved the final manuscript.

Conflict of Interest

There is no conflict of interest.

Acknowledgement

Authors give their acknowledgement to DST CURIE for providing the research support in this work.

References

[1] Negi, S., Mittal, P., Kumar, B., 2018. Impact of different layers on performance of OLED. Microsystem Technologies. 24, 4981-4989.

[2] Sharma, G., Hashmi, S.Z., Kumar, U., et al., 2020. Optical and electronic characteristics of ITO/NPB/Alq_3: DCJTB/Alq_3/Ag heterostructure based organic light emitting diode. Optik. 223, 165572.

[3] Ritu, Quraishi, A.M., Kattayat, S., et al., 2023. Optimization of NPD/Alq_3/TPBi/Bphen OLED structure and investigation of electrical characteristics along with allied parameters. Optical and Quantum Electronics. 55(8), 698.

[4] Sharma, G., Ritu, Quraishi, A.M., et al., 2022. Structure optimization and investigation of electrical and optical characteristics of Alq_3/TAZ: Ir (ppy) 3-BCP/HMTPD OLED. Optical and Quantum Electronics. 54(5), 284.

[5] Burroughes, J.H., Bradley, D.D., Brown, A.R., et al., 1990. Light-emitting diodes based on conjugated polymers. Nature. 347(6293), 539-541.

[6] Schwartz, G., Reineke, S., Rosenow, T.C., et al., 2009. Triplet harvesting in hybrid white organic Light-Emitting diodes. Advanced Functional Materials. 19(9), 1319-1333.

[7] Kuei, C.Y., Tsai, W.L., Tong, B., et al., 2016. Bis-tridentate Ir (III) complexes with nearly unitary RGB phosphorescence and organic light-emitting diodes with external quantum efficiency exceeding 31%. Advanced Materials. 28(14), 2795-2800.

[8] Ahmmed, S., Aktar, A., Ismail, A.B.M., 2021. Role of a solution-processed V_2O_5 hole extracting layer on the performance of CuO-ZnO-based solar cells. ACS Omega. 6(19), 12631-12639.

[9] Jiang, Y., Xiao, S., Xu, B., et al., 2016. Enhancement of photovoltaic performance by utilizing readily accessible hole transporting layer of vanadium (V) oxide hydrate in a polymer-fullerene blend solar cell. ACS Applied Materials & Interfaces. 8(18), 11658-11666.

[10] McElvain, J., Antoniadis, H., Hueschen, M.R., et al., 1996. Formation and growth of black spots in organic light-emitting diodes. Journal of Applied Physics. 80(10), 6002-6007.

[11] Burrows, P.E., Bulovic, V., Forrest, S.R., et al., 1994. Reliability and degradation of organic light emitting devices. Applied Physics Letters. 65(23), 2922-2924.

[12] Aziz, H., Xu, G., 1997. Electric-field-induced degradation of poly (p-phenylenevinylene) electroluminescent devices. The Journal of Physical Chemistry B. 101(20), 4009-4012.

[13] Kang, S.J., Park, D.S., Kim, S.Y., et al., 2002.

Enhancing the electroluminescent properties of organic light-emitting devices using a thin NaCl layer. Applied Physics Letters. 81(14), 2581-2583.

[14] Lai, S.L., Tao, S.L., Chan, M.Y., et al., 2010. Efficient white organic light-emitting devices based on phosphorescent iridium complexes. Organic Electronics. 11(9), 1511-1515.

[15] Brütting, W., 2005. Introduction to the physics of organic semiconductors. Physics of Organic Semiconductors. 1-14.

[16] Bronstein, H., Nielsen, C.B., Schroeder, B.C., et al., 2020. The role of chemical design in the performance of organic semiconductors. Nature Reviews Chemistry. 4(2), 66-77.

[17] Ugale, A., Kalyani, T.N., Dhoble, S.J., 2018. Potential of europium and samarium β-diketonates as red light emitters in organic light-emitting diodes. Lanthanide-based multifunctional materials. Elsevier: Amsterdam. pp. 59-97.

[18] Dangi, S.B., Hashmi, S.Z., Kumar, U., et al., 2022. Exploration of spectroscopic, surface morphological, structural, electrical, optical and mechanical properties of biocompatible PVA-GO PNCs. Diamond and Related Materials. 127, 109158.

[19] Dangi, S.B., Khichar, K.K., Kumar, U., et al., 2020. Investigation of optical properties of PVA-GO nanocomposites. AIP Conference Proceedings. 2220(1), 020082.

[20] Dhayal, V., Hashmi, S.Z., Kumar, U., et al., 2020. Spectroscopic studies, molecular structure optimization and investigation of structural and electrical properties of novel and biodegradable Chitosan-GO polymer nanocomposites. Journal of Materials Science. 55, 14829-14847.

[21] Heeger, A.J., 2010. Semiconducting polymers: The third generation. Chemical Society Reviews. 39(7), 2354-2371.

[22] Zhao, X., Zhan, X., 2011. Electron transporting semiconducting polymers in organic electronics. Chemical Society Reviews. 40(7), 3728-3743.

[23] Han, J.H., Kim, T.Y., Kim, D.Y., et al., 2021. Water vapor and hydrogen gas diffusion barrier characteristics of Al_2O_3-alucone multi-layer structures for flexible OLED display applications. Dalton Transactions. 50(43), 15841-15848.

[24] Obolda, A., Peng, Q., He, C., et al., 2016. Triplet-polaron-interaction-induced upconversion from triplet to singlet: A possible way to obtain highly efficient OLEDs. Advanced Materials. 28(23), 4740-4746.

[25] Carvelli, M., Janssen, R.A.J., Coehoorn, R., 2011. Determination of the exciton singlet-to-triplet ratio in single-layer organic light-emitting diodes. Physical Review B. 83(7), 075203.

[26] Chua, L.L., Zaumseil, J., Chang, J.F., et al., 2005. General observation of n-type field-effect behaviour in organic semiconductors. Nature. 434(7030), 194-199.

[27] Li, Y., Sonar, P., Murphy, L., et al., 2013. High mobility diketopyrrolopyrrole (DPP)-based organic semiconductor materials for organic thin film transistors and photovoltaics. Energy & Environmental Science. 6(6), 1684-1710.

[28] Yu, Z., Perera, I.R., Daeneke, T., et al., 2016. Indium tin oxide as a semiconductor material in efficient p-type dye-sensitized solar cells. NPG Asia Materials. 8(9), e305-e305.

[29] Bel Hadj Tahar, R., Ban, T., Ohya, Y., et al., 1998. Tin doped indium oxide thin films: Electrical properties. Journal of Applied Physics. 83(5), 2631-2645.

[30] Shaheen, S.E., Jabbour, G.E., Morrell, M.M., et al., 1998. Bright blue organic light-emitting diode with improved color purity using a LiF/Al cathode. Journal of Applied Physics. 84(4), 2324-2327.

[31] Schlaf, R., Parkinson, B.A., Lee, P.A., et al., 1998. Photoemission spectroscopy of LiF coated Al and Pt electrodes. Journal of Applied Physics. 84(12), 6729-6736.

[32] Ow-Yang, C.W., Jia, J., Aytun, T., et al., 2014. Work function tuning of tin-doped indium oxide electrodes with solution-processed lithium fluoride. Thin Solid Films. 559, 58-63.

[33] Aytun, T., Turak, A., Baikie, I., et al., 2012. Solution-processed LiF for work function tuning in electrode bilayers. Nano Letters. 12(1), 39-44.

[34] Turak, A., Huang, C.J., Grozea, D., et al., 2007. Oxidation of LiF-coated metal surfaces: Multilayer cathode structures as used for organic optoelectronics. Journal of the Electrochemical Society. 154(8), H691.

[35] Turak, A., Grozea, D., Huang, C., et al., 2012. Interfacial structure in organic optoelectronics. arXiv preprint arXiv:1208.0321.

[36] Turak, A., 2021. On the role of LiF in organic optoelectronics. Electronic Materials. 2(2), 198-221.

[37] Ahmed, S., Shaffer, J., Harris, J., et al., 2019. Simulation studies of non-toxic tin-based perovskites: Critical insights into solar performance kinetics through comparison with standard lead-based devices. Superlattices and Microstructures. 130, 20-27.

[38] Jahangir, K., Nowsherwan, G.A., Hussain, S.S., et al., 2021. Electrical simulation and optimization of ptb7: pc70bm based organic solar cell using gpvdm simulation software. ICRRD Quality Index Research Journal. 2, 131-140.

[39] Puspita, D., Syarifah, R.D., Rizal, N.S., 2022. GPVDM simulation of thickness effect on power conversion efficiency of PEDOT: PSS/P3HT: PCBM solar cell performance. AIP Conference Proceedings. 2663(1).

[40] Hima, A., Khechekhouche, A., Kemerchou, I., et al., 2018. GPVDM simulation of layer thickness effect on power conversion efficiency of $CH_3NH_3PbI_3$ based planar heterojunction solar cell. International Journal of Energetica. 3(1), 37-41.

[41] Li, Y., Sachnik, O., Van der Zee, B., et al., 2021. Universal Electroluminescence at voltages below the energy gap in organic light-emitting diodes. Advanced Optical Materials. 9(21), 2101149.

[42] Pu, Y.J., Chiba, T., Ideta, K., et al., 2015. Fabrication of organic light-emitting devices comprising stacked light-emitting units by solution-based processes. Advanced Materials. 27(8), 1327-1332.

[43] Cohen, E.R., Giacomo, P., 1987. Symbols, units, nomenclature and fundamental constants in physics. North-Holland: Amsterdam.

BILINGUAL PUBLISHING GROUP

Semiconductor Science and Information Devices
https://journals.bilpubgroup.com/index.php/ssid

ARTICLE

Sub-nano Layers of Li, Be, and Al on the Si(100) Surface: Electronic Structure and Silicide Formation

Victor Zavodinsky [*], ***Olga Gorkusha***

Khabarovsk Department of the Institute of Applied Mathematics, Far East Branch of the Russian Academy of Sciences, Khabarovsk, 690022, Russia

ABSTRACT

Within the framework of the density functional theory and the pseudopotential method, the electronic structure calculations of the "metal-Si(100)" systems with Li, Be and Al as metal coverings of one to four monolayers (ML) thickness, were carried out. Calculations showed that band gaps of 1.02 eV, 0.98 eV and 0.5 eV, respectively, appear in the densities of electronic states when the thickness of Li, Be and Al coverings is one ML. These gaps disappear with increasing thickness of the metal layers: first in the Li-Si system (for two ML), then in the Al-Si system (for three ML) and then in the Be-Si system (for four ML). This behavior of the band gap can be explained by the passivation of the substrate surface states and the peculiarities of the electronic structure of the adsorbed metals. In common the results can be interpreted as describing the possibility of the formation of a two-dimensional silicide with semiconducting properties in Li-Si(100), Be-Si(100) and Al-Si(100) systems.

Keywords: Kohn-Sham method; Pseudopotentials; Si(100) surface; Sub-nano metal layers; Density of states; Two-dimensional silicides; Semiconducting properties

1. Introduction

Metal layers on silicon have long attracted the attention of researchers. However, this mainly refers to layers of refractory 3d transition metals that form stable silicides. Layers of low-melting metals on silicon have not been studied enough.

The most indicative include works [1-10], where the atomic and electronic structure of the sub-nano

*CORRESPONDING AUTHOR:
Victor Zavodinsky, Khabarovsk Department of the Institute of Applied Mathematics, Far East Branch of the Russian Academy of Sciences, Khabarovsk, 690022, Russia; Email: vzavod@mail.ru

ARTICLE INFO
Received: 21 September 2023 | Revised: 27 October 2023 | Accepted: 30 October 2023 | Published Online: 1 November 2023
DOI: https://doi.org/10.30564/ssid.v5i1.5982

CITATION
Zavodinsky, V., Gorkusha, O., 2023. Sub-nano Layers of Li, Be, and Al on the Si(100) Surface: Electronic Structure and Silicide Formation. Semiconductor Science and Information Devices. 5(1): 11-17. DOI: https://doi.org/10.30564/ssid.v5i1.5982

COPYRIGHT
Copyright © 2023 by the author(s). Published by Bilingual Publishing Group. This is an open access article under the Creative Commons Attribution-NonCommercial 4.0 International (CC BY-NC 4.0) License. (https://creativecommons.org/licenses/by-nc/4.0/).

Li, Be and Al layers on Si(100) and Si(111) surfaces was studied. In the work of Kotllyar et al. [1], the high-temperature interaction of Al with the Si(100) surface at low coverages was studied using low-energy electron diffraction, Auger electron spectroscopy and scanning tunneling microscopy (STM). At low Al coverages (0.05-0.2 ML), the interaction of Al atoms with a top Si(100) substrate layer proceeds by two competitive mechanisms. The first mechanism prevails at Si(100) surface with a low density of missing-dimer defects and resides in the formation of the specific Al-Si clusters. The second mechanism is stimulated by the presence of missing-dimer defects and resides in the substitutional incorporation of Al atoms in the top Si(100) substrate layer. Both mechanisms result in the liberation of the surface Si atoms, which agglomerate into flat islands. In the work of Cocoletzi and Takeuchi [2], the first principles of total energy calculations of the Al induced Si(001)-(3×4) reconstruction are presented; the local density of state images was calculated and compared with the experimental STM measurement. Northrup [3] has studied the adatom-induced reconstruction of the Si(111)$\sqrt{3}\times\sqrt{3}$-Al surface using first-principles pseudopotential total-energy and force calculations. He proposed a new adatom model of this reconstruction wherein each Al adatom sits in a threefold-symmetric site with three first-layer Si neighbors and one second-layer Si neighbor directly below. For this model, the calculated dispersion of the adatom-induced surface states is in good agreement with the experiment. The work of Ko Young-Jo et al. [4] is of particular interest to us, since it describes first-principles calculations of the electronic structure of the Li-Si(100) system, which is one of the objects of our work. They find that Li adatoms interact mainly with the dangling-bond orbitals of Si dimers. The analysis of charge densities demonstrates a large charge transfer from the Li adatom to a dangling-bond orbital of a Si dimer, which is responsible for a large decrease in work function at submonolayer coverages. We will discuss their results in more detail below in comparison with ours. Rysbaev et al. [5] studied the formation of silicide films of metals (Li, Cs, Rb, and Ba) during ion implantation in Si and subsequent thermal annealing; the effect of ion implantation and subsequent heating on the frequency of surface and bulk plasma oscillations of valence electrons in silicon was described. Hite, Tang and Sprunger [6] used STM and photoelectron spectroscopy to investigate the nucleation, growth, and structure of beryllium on Si(111)-(7×7). They indicated that a chemical reaction occurs at temperatures as low as 120ºK, resulting in a nano-clustered morphology, presumed to be composed of a beryllium silicide compound. Upon annealing to higher temperatures, their data indicate that beryllium diffuses into the selvage region. Saranin et al. [7] studied ordered arrays of Be-encapsulated Si nanotubes on Si(111) surface using STM. Gordeev, Kolotova and Starikov [8] investigated the formation of metastable aluminum silicide as intermediate stage of Al-Si alloy crystallization. They noted that the mechanism of Al-Si alloy crystallization from an amorphous state is still unclear. Despite the absence of equilibrium compounds for this binary system, there are several experimental evidence confirming the formation of metastable silicide at annealing of amorphous Si mixed with Al. The authors considered the properties of the aluminum Al_2Si silicide structure, which is a probable candidate for the role of the observed metastable compound. Their investigation was based on the atomistic simulations with the interatomic potential and density functional theory approach. All used methods revealed that there are several crystal structures of Al_2Si with close geometry and relatively low formation energies. The chemical ordering in such structures is similar to the one in Si-Al melt. The authors also showed that the combination of these structures allows to form a crystal with different degrees of ordering. Terekhov et al. [9] have studied the possibility of the metastable Al_3Si phase formation in composite Al-Si films obtained by ion-beam and magnetron sputtering. Endo et al. [10] made an elementary analysis of each atom on the Si surface, and metal atoms on the Si(001) surface by STM and spectroscopy; the result was evaluated with the first principles calculations. As metallic contaminations, sub-monolayer of alu-

minum was evaporated on the Si(001)-2×1 surface. The local density of states on the Al/Si(001)-2×1 was measured by scanning tunneling spectroscopy at room temperature. Experimental results are in good agreement with those obtained from the calculations.

Unfortunately, we were unable to find publications (experimental or theoretical) concerning the electronic structure of the Be-Si(100) and Al-Si(100) systems. As for the Li-Si system, the work presents the results of calculations only for lithium layers of 0.5 and 1.0 ML and band gap of 1.35 eV width was found for one ML. However, almost all of the works listed above indicate the possibility of forming two-dimensional silicides when sub-nano layers of lithium, berlium and aluminum are deposited on the silicon surface. At the same time, there are publications indicating that two-dimensional silicides may have semiconductor properties. For example, in the work of Clark et al. [11] it was shown, as a result of calculations from first principles, that a nanolayer of the iron dislicide with a band gap of 0.73 eV can grow epitaxially on the Si(100) surface. The results indicate that the appearance of semiconductor properties is also possible when such a light metal as lithium is deposited on silicon, and it is necessary to check this possibility for other light metals, in particular for beryllium and aluminum. In order to clarify the possibility of silicide formation with semiconductor properties in Li-Si(100), Be-Si(100) and Al-Si(100) nanosystems, we fulfilled the study of these systems by computer simulation using the Kohn-Sham method [12] within the framework of the density functional theory [13] and the pseudopotential method [14]. Since this approach involves performing calculations only at 0°K, we considered these systems with disordered metal layers.

2. Research methodology

All calculations were performed using the FHI96md package [15]. Pseudopotentials were found using the FHI98pp package [14]. To calculate the exchange-correlation energy, the local electron density approximation was used [16,17]. In all cases, the cutoff energy of a set of plane waves was taken to be 14 Ry; calculations were carried out with the five k-points: (0.5; 0.5; 0.5), according to the 3 × 3 × 1 scheme, in a supercell with dimensions 14.54 × 14.54 × 40 (all values are given in atomic units, one atomic unit is equal to 0.529 Å). The electronic structure was studied by calculating the density of electronic states (DOS), for which each electronic level was smeared using a Gaussian function with a half-width of 0.05 eV or 0.025 eV. The last half-width was used in cases with a narrow band gap. We took a Si slab consisting of four monolayers (ML) as a silicon substrate with a Si(100) surface. Each ML contained four atoms, and the lowest ML was terminated with eight hydrogen atoms. Thus, due to the periodic boundary conditions in the X and Y directions, we studied a thin infinite plate, and the large value of the parameter c (40 atomic units) for the supercell ensures that there is no interaction between the virtual plates in Z dimension.

The atoms of the lowest ML of silicon were fixed; the atoms of the remaining layers, as well as the ML atoms of the studied metals, could move under the action of quantum mechanical interatomic forces.

Each metal ML also contained four atoms. Their deposition was carried out in a disordered manner using a special program developed by us based on a random number generator. To make sure that the band gap arises precisely during the interaction of silicon with metal, we also calculated the DOS for metal layers taken separately from the silicon substrate.

3. Results and discussion

Our calculations showed that for the metals studied, the arrangement of their atoms on the Si(100) surface turned out to be rather different. Schemes of the optimized arrangement of atoms for one ML metal-Si(100) system are presented in **Figure 1**.

It can be seen that, under the influence of the structure of the silicon surface, some ordering of the arrangement of metal atoms occurred, but in all cases, the structure of the metal monolayers is still far from epitaxial. The structure of systems with a greater number of monolayers than one ML became

increasingly disordered with increasing thickness.

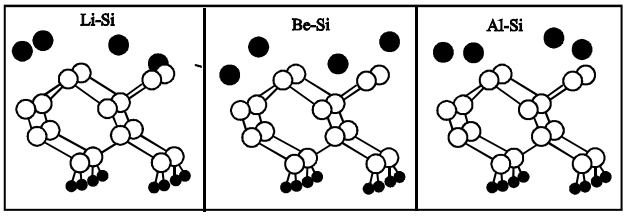

Figure 1. Arrangement of atoms in the Li-Si, Be-Si and Al-Si systems when the first disordered metal monolayers are deposited on the Si(100) surface. White circles are silicon atoms, big black circles are metal atoms, small black circles are hydrogen atoms.

Figure 2 shows the distribution patterns of the density of states formed when the first monolayers of Li, Be and Al are deposited on the surface. The DOS for a clean Si(100)-2×1 surface with the gap of 0.35 eV is also shown there. Note that the reconstruction of the surface structure Si(100)→Si(100)-2×1 occurred spontaneously during the relaxation of the free Si(100) surface, and during calculations with adsorbed metal layers, the reconstruction disappeared.

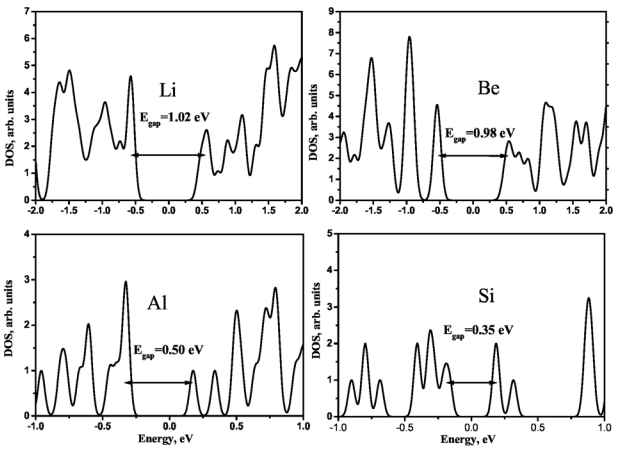

Figure 2. Density of electronic states formed when the first monolayer of Li, Be and Al is deposited on the Si(100) surface in comparison with the density of states for a clean Si(100)-2×1 surface. The Fermi level corresponds to zero energy.

From this figure, it is clear that in all cases there is an energy gap near the Fermi level: 1.02 eV for Li-Si, 0.98 eV for Be-Si and 0.50 eV for Al-Si. The band gap we obtained for the Li-Si system is significantly less than the 1.35 eV value [4]. This can be explained by the fact that Ko et al. provide data for an ordered Li monolayer on Si(100), while we examined the Li-Si(00) system with a disordered monolayer of Li. For the clean Si(100)-2×1 surface, we obtained 0.35 eV in good agreement with the known data given in published works: 0.4 eV (electron energy loss spectroscopy) [18], 0.5 eV (scanning tunneling spectroscopy) [19], and 0.2-0.3 eV (calculations from first principles) [20]. At the same time, we did not detect an energy gap in the electronic structure of Li, Be and Al metal monolayers without a silicon substrate (**Figure 3**). Unfortunately, we do not have data on the electronic structure of Be-Si(100) and Al-Si(100) systems, so we cannot compare our results with published ones. However, since our results for pure silicon and for lithium on silicon are close to those published, we have reason to believe that the results we obtained for the Be and Al on Si(100) are also quite reliable.

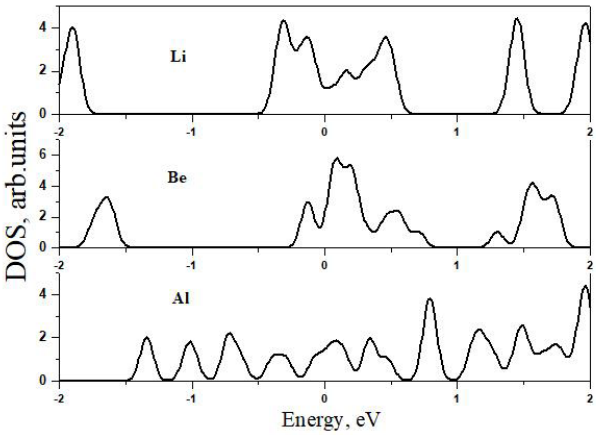

Figure 3. DOS corresponding to monolayers of Li, Be and Al taken separately from the silicon substrate.

The deposition of the second ML led to the fact that in the Li-Si system, the gap in the density of states disappeared. In the Be-Si system, it decreased to 0.61 eV, and in the Al-Si system, it increased to 0.62 eV, which is illustrated in Figure 4 (top panels). In contrast, the DOS for two ML of Li, Be and Al without a substrate has a metallic character, as can be seen in the same figure (bottom panels), as in the case of a single ML.

We did not examine the Li-Si system during the deposition of the third ML, since we were interested in the presence of an energy gap, and in this system the gap disappeared already with two metal ML.

The DOS for the Be-Si and Al-Si systems are shown in **Figure 5** (top panels). In the Be-Si system, the gap decreased to 0.27 eV, and in the Al-Si system, it completely disappeared. Calculation of three monolayers of beryllium and aluminum separately from silicon demonstrated the metallic nature of their DOS (see **Figure 5**, bottom panels).

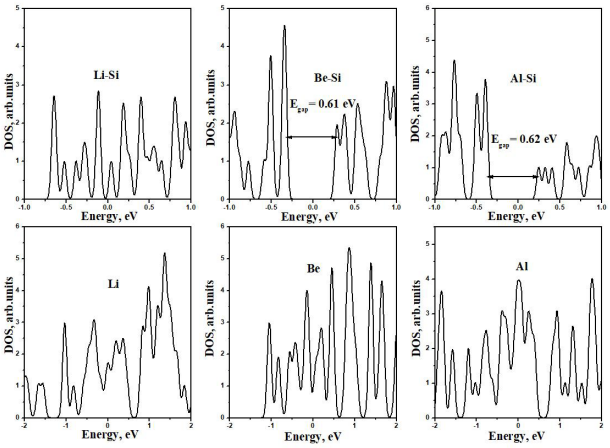

Figure 4. Densities of states of Li-Si, Be-Si and Al-Si systems for two metal monolayers. On the bottom panels there is a DOS for two monolayers of Li, Be and Al, taken separately from the silicon substrate.

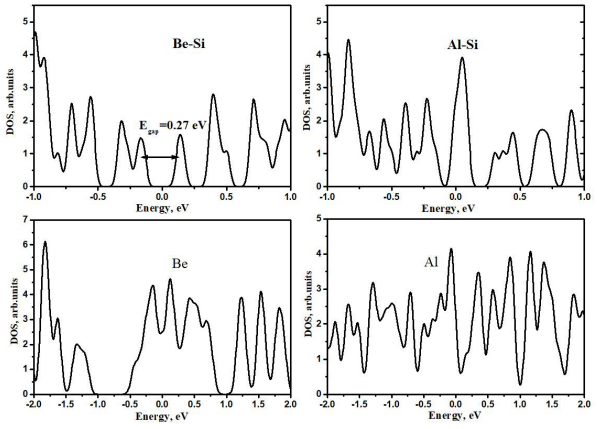

Figure 5. DOS for Be-Si and Al-Si systems with three metal monolayers. Here (on the bottom panels) is a DOS for three monolayers of Be and Al, taken separately from the substrate.

To find out whether the energy gap in the Be-Si system will disappear when another (fourth) Be monolayer is deposited on the silicon surface, we carried out the corresponding calculations and plotted the density of states in **Figure 6**.

From this figure, it is clear that the DOS for the Be-Si system with four ML of beryllium has a metallic character.

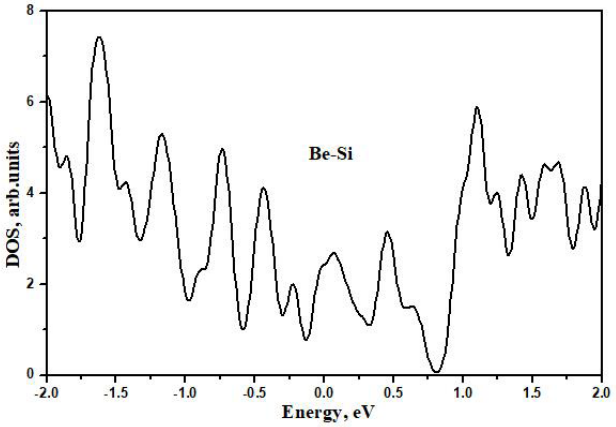

Figure 6. DOS for the Be-Si system with four metal monolayers.

Thus, the obtained results show that in disordered Li-Si(100), Be-Si(100) and Al-Si(100) systems with sub-nano metal layers, electronic structures with band gaps are formed, and the bands disappear with increasing thickness of the deposited metal layers.

4. Conclusions

Electronic structure calculations by the Kohn-Sham method using pseudopotentials showed that in the densities of electronic states of two-dimensional "metal-Si(100)" systems with Li, Be and Al disordered layers of the one ML thickness, band gaps with widths of 1.02 eV, 0.98 eV and 0.5 eV, respectively, appear. These gaps disappear with increasing thickness of the metal layers: first in the Li-Si system (for two ML), then in the Al-Si system (for three ML) and then in the Be-Si system (for four ML).

It seems to us that our results can be interpreted as the discovery of the possibility of forming two-dimensional silicides of lithium, beryllium and aluminum with semiconducting properties. This assumption correlates with the conclusions expressed in the works we cited in the Introduction.

Typically, the formation of silicides is accompanied by mixing of metal and silicon atoms. In our case, mixing does not occur, which is apparently explained by the zero temperature of the calculation. However, there is another important characteristic of silicides that should manifest itself in two-di-

mensional silicides, namely the formation of strong chemical bonds between the metal layers and the silicon surface atoms. The energy value characterizing the magnitude of these forces is the adhesion energy. We calculated the adhesion energy (E_{adh}) and obtained the following values: E_{adh}(Li) = 1.67 J/m^2, E_{adh}(Be) = 1.68 J/m^2, E_{adh}(Al) = 2.05 J/m^2. For comparison, we carried out test calculations for 1 ML Fe on the surface of Si(100), and obtained an adhesion energy of 4.5 J/m^2, which is 2-2.5 times higher than our values. Perhaps this is because iron has 8 valence electrons versus 1, 2 and 3 in Li, Be and Al. Besides, when the thickness of the metal layer becomes greater, its non-order increases, which also affects the decrease in the band gap. Therefore, in our case, the values of adhesion energy are sufficient to form two-dimensional silicides. In our opinion, such systems can be used to create two-dimensional semiconductor devices.

Authors' Contributions

Victor Zavodinsky: concept, review, discussion of results, writing the article.

Olga Gorkusha: performing calculations, constructing figures, discussing the results.

Conflict of Interest

The authors have no conflict of interest with anyone.

References

[1] Kotlyar, V.G., Saranin, A.A., Zotov, A.V., et al., 2002. High-temperature interaction of Al with Si(100) surface at low Al coverages. Surface Science. 506(1-2), 80-86.
DOI: https://doi.org/10.1016/S0039-6028(01)01768-X

[2] Cocoletzi, G.H., Takeuchi, N., 2002. First principles total energy calculations of the Al induced Si (0 0 1)-(3×4) reconstruction. Surface Science. 504, 101-107.
DOI: https://doi.org/10.1016/S0039-6028(01)01915-X

[3] Northrup, J.E., 1984. Si(111)√3×√3-Al: An adatom-induced reconstruction. Physical Review Letters. 53(7), 683-686.
DOI: https://doi.org/10.1103/PhysRevLett.53.683

[4] Ko, Y.J., Chang, K.J., Yi, J.Y., 1997. Atomic and electronic structure of Li-adsorbed Si(100) surfaces. Physical Review B. 56(15), 9575.
DOI: https://doi.org/10.1103/PhysRevB.56.9575

[5] Rysbaev, A.S., Normurodov, M.T., Khujaniyozov, J.B., et al., 2021. On the formation of silicide films of metals (Li, Cs, Rb, and Ba) during ion implantation in Si and subsequent thermal annealing. Journal of Surface Investigation: X-ray, Synchrotron and Neutron Techniques. 15(3), 607-610.
DOI: https://doi.org/10.1134/S10274510210303

[6] Hite, D.A., Tang, S.J., Sprunger, P.T., 2003. Reactive epitaxy of beryllium on Si (1 1 1)-(7×7). Chemical Physics Letters. 367(1-2), 129-135.
DOI: https://doi.org/10.1016/S0009-2614(02)01637-8

[7] Saranin, A.A., Zotov, A.V., Kotlyar, V.G., et al., 2004. Ordered arrays of Be-encapsulated Si nanotubes on Si (111) surface. Nano Letters. 4(8), 1469-1473.

[8] Gordeev, I., Kolotova, L., Starikov, S., 2022. Formation of metastable aluminum silicide as intermediate stage of Al-Si alloy crystallization. Scripta Materialia. 210, 114481.
DOI: https://doi.org/10.1016/j.scriptamat.2021.114481

[9] Terekhov, V.A., Usoltseva, D.S., Serbin, O.V., et al., 2018. Possibility of the metastable Al_3Si phase formation in composite Al-Si films obtained by ion-beam and magnetron sputtering. Condensed Matter and Interphases. 20(1), 135-147.
DOI: https://doi.org/10.17308/kcmf.2018.20/485

[10] Endo, K., Arima, K., Kataoka, T., et al., 1998. STM/STS and the first principles calculations on Al/Si (001) 2×1. Applied Physics A. 66, S145-S148.
DOI: https://doi.org/10.1007/s003390051118

[11] Clark, S.J., Al-Allak, H.M., Brand, S., et al., 1998. Structure and electronic properties of $FeSi_2$. Physical Review B. 58(16), 10389.
DOI: https://doi.org/10.1103/PhysRevB.58.10389

[12] Kohn, W., Sham, L.J., 1965. Self-consistent equations including exchange and correlation effects. Physical Review. 140(4A), A1133.
DOI: https://doi.org/10.1103/PhysRev.140.A1133

[13] Hohenberg, P., Kohn, W., 1964. Inhomogeneous electron gas. Physical Review. 136(3B), B864.
DOI: https://doi.org/10.1103/PhysRev.136.B864

[14] Fuchs, M., Scheffler, M., 1999. Ab initio pseudopotentials for electronic structure calculations of poly-atomic systems using density-functional theory. Computer Physics Communications. 119(1), 67-98.
DOI: http://dx.doi.org/10.1016/S0010-4655(98)00201-X

[15] Bockstedte, M., Kley, A., Neugebauer, J., et al., 1997. Density-functional theory calculations for poly-atomic systems: Electronic structure, static and elastic properties and ab initio molecular dynamics. Computer Physics Communications. 107(1-3), 187-222.
DOI: http://dx.doi.org/10.1016/S0010-4655(97)00117-3

[16] Ceperley, D.M., Alder, B.J., 1980. Ground state of the electron gas by a stochastic method. Physical Review Letters. 45(7), 566.
DOI: https://doi.org/10.1103/PhysRevLett.45.566

[17] Perdew, J.P., Zunger, A., 1981. Self-interaction correction to density-functional approximations for many-electron systems. Physical Review B. 23(10), 5048.
DOI: https://doi.org/10.1103/PhysRevB.23.5048

[18] Gavioli, L., Betti, M.G., Cricenti, A., et al., 1995. Surface electronic structure at Si (100)-(2x1). Journal of Electron Spectroscopy and Related Phenomena. 76, 541-545.

[19] Hata, K., Shibata, Y., Shigekawa, H., 2001. Fine electronic structure of the buckled dimers of Si(100) elucidated by atomically resolved scanning tunneling spectroscopy and bias-dependent imaging. Physical Review B. 64(23), 235310.
DOI: https://doi.org/10.1103/PhysRevB.64.235310

[20] Fritsch, J., Pavone, P., 1995. Ab initio calculation of the structure, electronic states, and the phonon dispersion of the Si(100) surface. Surface Science. 344(1-2), 159-173.
DOI: https://doi.org/10.1016/0039-6028(95)00802-0

BILINGUAL PUBLISHING GROUP

Semiconductor Science and Information Devices
https://journals.bilpubgroup.com/index.php/ssid

ARTICLE

Analysis of the Effect of Radiation Defects by Low-energy Protons on Electrophysical Properties of Silicon N^+-P-P^+ Structure

Bogatov N.M. [*], ***Grigoryan L.R., Kovalenko M.S., Volodin V.S.***

Department of Physics and Information Systems, Kuban State University, Krasnodar, 350040, Russia

ABSTRACT

Nowadays, radiation engineering is a promising direction in the creation of semiconductor devices. The proton irradiation is used to controllably change the optical, electrical, recombination, mechanical and structural properties of the semiconductors. Low-energy protons make it possible to purposefully change material properties near the surface where the n^+-p junction is located. In this paper, the impact of low-energy protons on the electro physical parameters of n^+-p-p^+ silicon photoelectric converters (SPC) is analyzed. The current-voltage characteristics and switching time of these SPCs are measured. The switching time is determined using rectangular bipolar voltage pulses with an amplitude of 10 mV, a frequency of 200 kHz, or a frequency of 1 MHz. A theoretical and experimental analysis of the obtained results is performed. The comparison of experimental data with the results of calculations shows that protons with an energy of 180 keV and a dose of 10^{15} cm^{-2} create two regions in the space charge region of the n^+-p junction with different switching times of 4.2×10^{-7} s and 5.5×10^{-8} s. SPC frequency characteristics have been improved by reducing the effective lifetime by 5-10 times. This effect can be used to create high-speed photodiodes with an operating modulation frequency of 18 MHz.

Keywords: Silicon; n^+-p junction; Lifetime; Proton; Pulse characteristic

1. Introduction

The relevance of studies of the effects of ionizing radiation on the properties of semiconductor materials and devices is increasing due to the increasing use of these processes in industrial technologies un-

*CORRESPONDING AUTHOR:
Bogatov N.M., Department of Physics and Information Systems, Kuban State University, Krasnodar, 350040, Russia; Email: bogatov@phys.kubsu.ru

ARTICLE INFO
Received: 8 September 2023 | Revised: 1 November 2023 | Accepted: 3 November 2023 | Published Online: 10 November 2023
DOI: https://doi.org/10.30564/ssid.v5i1.6014

CITATION
Bogatov, N.M., Grigoryan, L.R., Kovalenko, M.S., et al., 2023. Analysis of the Effect of Radiation Defects by Low-energy Protons on Electrophysical Properties of Silicon N^+-P-P^+ Structure. Semiconductor Science and Information Devices. 5(1): 18-25. DOI: https://doi.org/10.30564/ssid.v5i1.6014

COPYRIGHT
Copyright © 2023 by the author(s). Published by Bilingual Publishing Group. This is an open access article under the Creative Commons Attribution-NonCommercial 4.0 International (CC BY-NC 4.0) License. (https://creativecommons.org/licenses/by-nc/4.0/).

der controlled exposure, as well as the use of devices under uncontrolled environmental exposure [1-6].

The electrophysical characteristics of semiconductor structures with an n^+-p junction depend on the volume and surface recombination rates, the impurities and radiation defects distributions. The parameters of volume and surface recombination were measured by the photoconductivity decay method [7,8]. Methods for determining recombination parameters are being improved. Pulsed illumination was used to determine the effect of structural defects on recombination parameters in the bulk of polycrystalline silicon and the p-n junction [9]. Measuring recombination parameters using the photoconductivity method, which is recorded using microwave radiation, allows you to monitor the results of technological processes [10].

The transient characteristics of semiconductor devices can be improved by irradiating them with protons [11]. The influence of irradiation with low-energy protons and the temperature of irradiated samples on the parameters of current-voltage characteristics (CVC) of silicon photoelectric converters (SPC) and the distribution of radiation defects is shown in articles [12,13]. As a result of irradiation with low energy protons, the switching time of SPC decreases [14]. The authors of the article [15] draw attention to the relevance of numerical modeling of the effects of irradiation with light and ionizing particles in semiconductor devices.

From a scientific and practical point of view, it is necessary to study the change in the electrical properties of SPCs under the influence of low-energy protons and evaluate the possibility of reducing their switching time in a dynamic mode.

2. Research methods

Photoelectric converters are a wide class of devices that convert the energy of electromagnetic radiation into electrical energy [16-18]. These devices include the semiconductor photoelectric converter that performs the functions of a primary converter. The frequency characteristics of photovoltaic converters depend on the switching time of the semiconductor photoelectric converters.

The subject of the study is the properties of n^+-p-p^+ SPCs. The samples' parameters: concentration of equilibrium holes in the base—$p_0 \approx 10^{15}$ cm^{-3}, thickness of diffusion n^+-p and p-p^+ layers—$d_n \approx d_p \approx$ 0.45 μm, base thickness—$L \approx 200$ μm, area—$S \gg 1$ cm^2, phosphorus concentration on the surface of n^+ layer—$N_P \approx 10^{20}$ cm^{-3}, boron concentration on the surface of p^+ layer—$N_B \approx 10^{20}$ cm^{-3}.

Proton irradiation was performed from the n^+ layer side. Radiation dose $F_p = 10^{15}$ cm^{-2}. Sample irradiation conditions (proton energy E_p, sample temperature Tp): N1 – E_p = 180 keV, Tp = 83 K; N2 – E_p = 40 keV, Tp = 83 K; N3 – E_p = 40 keV, T_p = 300 K. The control group of 7 samples with very similar electrophysical characteristics N4 was not irradiated.

The dark CVC of the SPC was measured using an IPP1 device at a temperature T = 300 K [12,13] (**Figure 1**).

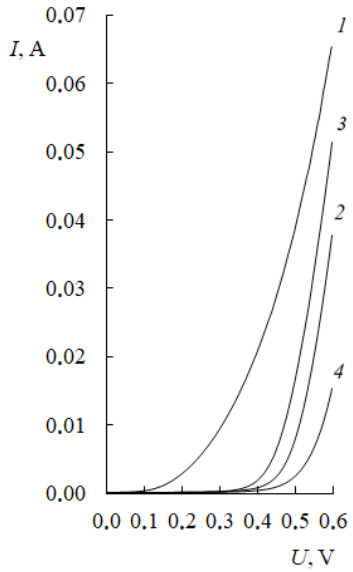

Figure 1. CVC of the studied SPC.

Note: 1—N1, 2—N2, 3—N3, 4—N4.

Transient characteristics were measured in the dark using a DSOX2022A digital oscilloscope, including the functions of a voltage pulse generator and a multimeter [14], using bipolar rectangular voltage pulses with a constant amplitude Um = 10 mV and a frequency f = 200 kHz and f = 1 MHz. The measured dependences of voltage U on time t are shown in **Figures 2 and 3**.

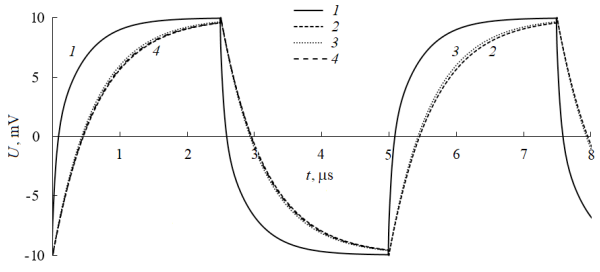

Figure 2. Transient characteristics of the SPC at a frequency 200 kHz.

Note: 1—N1, 2—N2, 3—N3, 4—N4.

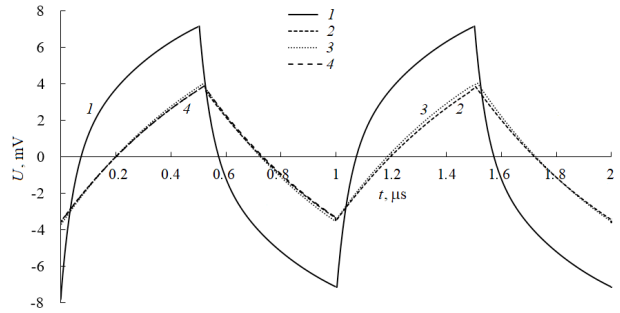

Figure 3. Transient characteristics of the SPC at a frequency 1 MHz.

Note: 1—N1, 2—N2, 3—N3, 4—N4.

3. Analysis of the research results

The depth distributions of the average number of interstitial silicon G_{Si}, vacancies G_V, and divacancies G_W created by one proton per unit of the projective path length were calculated using the model of the formation of primary radiation defects (PRD) [19] (**Figure 4**). The rate of formation of radiation defects depends on the concentration of impurities and the temperature of the samples [12,13,19,20].

Protons with E_p = 40 keV create PRDs in the n^+ layer at a depth of 0.41 μm. In this case, the number of PRDs at T_p = 300 K is several times greater than at T_p = 83 K, as well as the number of PRDs created by protons with E_p = 180 keV at T_p = 83 K (**Figure 4**). Protons with E_p = 40 keV change the properties of the n^+ layer, so the CVC of the irradiated samples N2, N3 and the unirradiated sample N4 are different (**Figure 1**). However, the transient characteristics of these samples differ little. Consequently, they do not depend on the electrical properties of the n^+ layer.

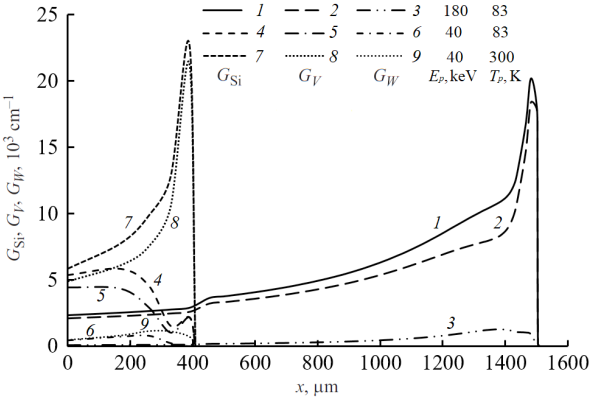

Figure 4. The distributions of PRD created by a proton with energy E_p at the temperature T_p of the irradiated SPC.

Protons with E_p = 180 keV create PRDs in the SCR of the n^+-p junction up to 1.51 μm (**Figure 4**). PRDs are absent in the base of SPC under these irradiation conditions. The transient characteristics of SPC N1 differ from the transient characteristics of SPC N2, N3, N4 (**Figures 2 and 3**), therefore the transient characteristics of the SPCs are determined by the parameters of the radiation-damaged SCR of the n^+-p junction. The CVC of SPC N1 differs from the CVC of SPC N2, N3, N4 (**Figure 1**), which is explained by a change in the electrophysical characteristics of the SCR of SPC N1 under proton irradiation.

Shockley [21] proposed the fundamental system of differential equations (FSDE) for the analysis of the transport of charge carriers in semiconductors with n^+-p junction.

$$\begin{cases} \vec{j}_n = \mu_n n \vec{\nabla}\varphi - D_n \vec{\nabla} n \\ 0 \\ \vec{j}_p = -\mu_p p \vec{\nabla}\varphi - D_p \vec{\nabla} p \\ 0 \\ \dfrac{\partial n}{\partial t} + \left(\vec{\nabla}; \vec{j}_n\right) = G - R \\ 0 \\ \dfrac{\partial p}{\partial t} + \left(\vec{\nabla}; \vec{j}_p\right) = G - R \\ 0 \\ \Delta\varphi = -\dfrac{q}{\varepsilon\varepsilon_0}(p - n + N_D^+ - N_A^-) \\ 0 \end{cases} \quad (1)$$

The system of equations, (1) contains unknown variables: n—the concentrations of electrons, p—the

concentrations of holes, $\vec{j}_n$—the density of the electron flow, $\vec{j}_p$—the density of the hole flow, φ—the potential of the internal electric field; specified silicon parameters: μ_n—mobility of the electrons, D_n—diffusion coefficient of the electron, μ_p—mobility of the holes, D_p—diffusion coefficient of the hole, G—the rate of volume generation of the electron-hole pairs, R—the rate of volume recombination of the electron-hole pairs, N_D^+—concentration of the ionized donors, N_A^-—concentration of the ionized acceptors, q—elementary charge, ε—permittivity, ε_0—dielectric constant.

From the system of equations, (1) follows the dependence of the electric current I on the voltage U_{np} at the *n-p* junction of the following form [22].

$$I = I_0\left[\exp\left(\frac{qU_{np}}{kT}\right) - 1\right] + I_r\left[\exp\left(\frac{qU_{np}}{akT}\right) - 1\right] + \frac{U_{np_s}}{R_{sh}} \quad (2)$$

$$U_{np} = U - IR_s \quad (3)$$

where I_0—reverse saturation current due to quasi-neutral n^+ layer and base; I_r—recombination current due to SCR; a—the coefficient of nonideality of the *n-p* junction; R_{sh}—shunting resistance of the *n-p* junction; U—electrical voltage at the contacts; R_s—concentrated sequential resistance; k—Boltzmann constant. It is necessary to determine which region of the SPC gives the main contribution to the experimental dependences CVC. For this purpose, the experimental dependencies $I(U)$ (**Figure 1**) must be approximated by a theoretical dependence (4).

$$I = I_0\left(\exp\left\{\frac{e(U - IR_s)}{akT}\right\} - 1\right) + \frac{U - IR_s}{R_{sh}} \quad (4)$$

The parameters of CVC calculated as a result of the approximation are given in the table. The nonideality coefficient of the *n-p* junction $a = 1.6$ for the non-irradiated sample N4 (table). It means that the SCR gives the main contribution to the CVC at the voltage $U < 0.6$ V [22].

Radiation defects created by protons with energy 180 keV disrupt the structure of the SCR and reduce the lifetime of the electrons and holes. Therefore, the contribution of the SCR to the CVC and the nonideality coefficient increase, so that $a = 2.6$ for sample N1 (table).

Radiation defects created by protons with energy 40 keV change the properties of the *n*-region so that the concentration of the electrons, the diffusion length and the lifetime of the holes are reduced. As a result, the contribution of the *n*-region to the CVC increases. The quasineutral region contributes to the CVC with a non-ideality coefficient $a = 1$ [22]. Therefore, for samples N2 and N3 the coefficient of nonideality a is close to 1 (table).

The value of I_{0r} in sample N2 is an order of magnitude less than in sample N3 (table), because G_{Si}, G_V, created in the *n*-region at $T_p = 83$ K, are smaller than at $T_p = 300$ K (**Figure 4**).

The irradiated SPCs have less value of R_s than the non-irradiated ones, which is apparently due to a decrease in the resistance of surface. The decrease of R_{sh} in irradiated SPCs may be caused by an increase in the number of surface states at the ends of the *n-p* junction.

When measuring the pulse characteristics, the condition of the small amplitude of the voltage at the contacts was fulfilled (5).

$$qU_m/kT < 1 \quad (5)$$

Inequality (5) means that a mode of low injection of nonequilibrium electrons and holes in the n^+ and p regions is realized. According to the experimental conditions, there is no light generation of electrons and holes $G = 0$. Then the FSDE (1) is simplified so that the solution for the concentration of electrons and holes has the form (6).

$$n = n_0 + \delta n,\ p = p_0 + \delta p \quad (6)$$

where n_0 and p_0 are the solution of the system (1) under the equilibrium conditions $\vec{j}_n = 0$, $\vec{j}_p = 0$. To determine δn, δp we use substitution.

$$\delta n(x, t) = \sum_i \left[A_{ni}(x) - B_{ni}(x) \cdot \exp\left(-\frac{t - t_0}{\tau_i}\right) - 1\right] \quad (7)$$

$$\delta p(x, t) = \sum_i \left[A_{pi}(x) - B_{pi}(x) \cdot \exp\left(-\frac{t - t_0}{\tau_i}\right) - 1\right] \quad (8)$$

where $t_0 < t < t_m$, $t_m - t_0 = (2f)^{-1}$. The functions $A_{ni}(X)$, $B_{ni}(X)$, $A_{pi}(X)$, $B_{pi}(X)$ are the solution of FSDE in quasi-neutral *p*, n^+ regions and SCR.

The range of switching time values $\tau_j \in (2\Delta t, (4f)^{-1})$ is determined by the duration of the bipolar voltage pulses $(2f)^{-1}$ and the signal sampling step Δt. The SPC SCR makes the main contribution to the voltage drop U [22]. Thus, electrical voltage relaxation processes occur in the SPC with an effective lifetime τ_j depending on the processes in the SCR.

$$U(t) = \sum_j \left[D_j \cdot \exp\left(-\frac{t - t_0}{\tau_j} \right) - C_j \right], \text{ when } t_0 < t < t_m. \quad (9)$$

When using the dependence (9), the approximation of the pulse characteristics (**Figures 2 and 3**) gives close values of the effective lifetime in the SCR for the samples N2, N3, N4 (**Table 1**). Two values $\tau_1 = 4.2 \times 10^{-7}$ s, $\tau_2 = 5.5 \times 10^{-8}$ s were found for sample N1.

Consequently, the structure of SPC was changed by protons with an energy of 180 keV so, there are two regions in SCR with different values τ_1 and τ_2. The lifetime τ_2 belongs to the region with a high concentration of the PRD near the Bragg peak at $x = 1.48$ mm (**Figure 4**).

The transient response simulation results are shown in **Figures 5-7**. A decrease of lifetime τ at a given pulse frequency $f = 10$ MHz causes a change in the shape of the transient response. Transient characteristics have a triangular shape with a smaller amplitude and equal length front and rear wave fronts (**Figure 5**) at the values of the parameters $\tau = 2.5 \times 10^{-7}$ s and $\tau = 5 \times 10^{-7}$ s.

A decrease of the τ value at the frequency $f = 10$ MHz reestablishes the shape of the transient characteristics: A reduction of 10 times gives the transient characteristics shown in **Figure 6**, and 50 times the transient characteristics shown in **Figure 7**.

Table 1. Electrophysical parameters of SPC.

Sample, N	I_{0r}, A	a	R_s, Ohm	R_{sh}, Ohm	t, s
1	1.6×10^{-4}	2.6	3.1	1.2×10^{5}	4.2×10^{-7}; 5.5×10^{-8}
2	1.6×10^{-9}	1.2	2.3	1.1×10^{5}	6.6×10^{-7}
3	1.5×10^{-8}	1.3	2.2	1.1×10^{5}	6.3×10^{-7}
4	1.6×10^{-8}	1.6	4.2	3.4×10^{5}	6.4×10^{-7}

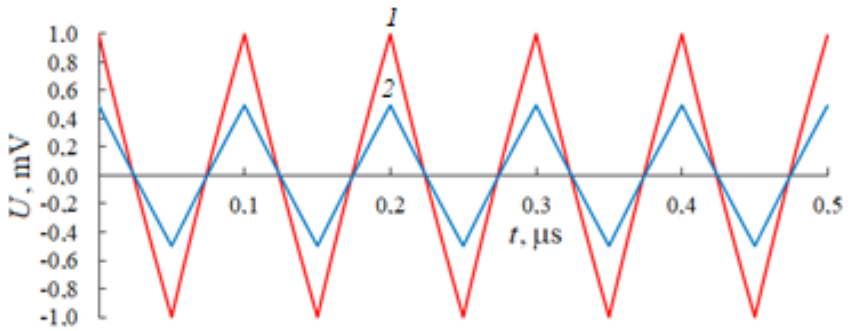

Figure 5. The transient characteristics at pulse frequency $f = 10$ MHz. The lifetime in SCR is *1* – $\tau = 2.5 \times 10^{-7}$ *s*, *2* – $\tau = 5 \times 10^{-7}$ *s*.

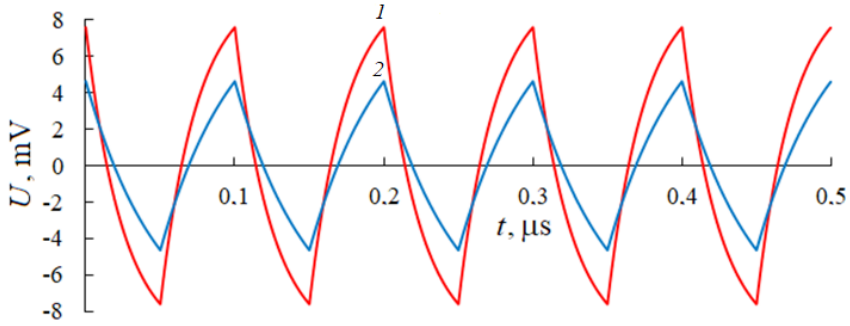

Figure 6. The transient characteristics at pulse frequency $f = 10$ MHz. The lifetime in SCR is *1* – t = 0.25×10^{-7} *s*, *2* – t = 0.5×10^{-7} *s*.

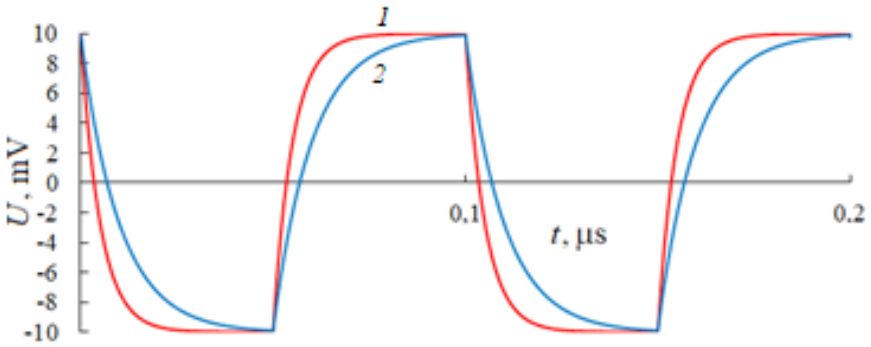

Figure 7. The transient characteristics at pulse frequency f = 10 MHz. The lifetime in SCR is *1* – $\tau = 0.05 \times 10^{-7}$ *s, 2* – $\tau = 0.1 \times 10^{-7}$ *s.*

4. Conclusions

Proton irradiation makes it possible to locally create the electrically and recombinationally active defects in semiconductors with a maximum concentration in the Bragg peak region. Radiation defects created by protons with an energy 180 keV and a dose 10^{15} cm^{-2} disrupt the structure of the SCR of the n^+-p junction of silicon devices and reduce the lifetime of charge carriers, which leads to a significant increase in the contribution of SCR to the dark electric current in stationary mode. It was found that two regions with different values of effective lifetimes $\tau_1 = 4.2 \times 10^{-7}$ s, $\tau_2 = 5.5 \times 10^{-8}$ s were formed in the SCR under the exposure of the proton irradiation. The value of τ_2 is an order of magnitude less than in non-irradiated devices.

Based on the results of the simulation of transient characteristics, it can be concluded that in order to improve the frequency characteristics at a frequency 10 MHz the effective lifetime should be reduced by 5 ÷ 10 times. However, in this case, an increase in the dose by 10 times will not lead to an inversely proportional decrease in the effective lifetime. The reason is that the concentration of formed PRDs in the Bragg peak region is much higher than the concentration of the main impurities in silicon grown by the Czochralski method (phosphorus, boron, oxygen, carbon) and other defects interacting with PRD at the stage of formation of secondary radiation defects (SRD). Therefore, direct or indirect annihilation of interstitial silicon and vacancies limits the concentration of recombination active SRDs. Consequently, the task of improving of the frequency characteristics of semiconductor devices cannot be solved only by increasing the radiation dose, but must be solved in combination with the formation of the semiconductor structure and impurity composition.

Author Contributions

Bogatov N. M.—problem statement, research management, article writing.

Grigoryan L. R.—transient response measurement.

Kovalenko M. S.—modeling and calculations.

Volodin V. S.—CVC measurement.

Conflict of Interest

The authors declare no conflict of interest.

Acknowledgement

We thank Yu.A. Agafonov and V.I. Zinenko (Institute of Microelectronics Technology and High Purity Materials of the Russian Academy of Sciences) for irradiation of the samples.

References

[1] Abdullaeva, I.A., Abdinova, G.D., Tagiyev, M.M., et al., 2021. Effect of gamma irradiation

on the electrical properties of extruded $Bi_{85}Sb_{15}$<Te> samples. Inorganic Materials. 57, 887-892.

[2] Li, J., Aierken, A., Liu, Y., et al., 2021. A brief review of high efficiency III-V solar cells for space application. Frontiers in Physics. 8, 631925.

[3] Siddiqui, A., Usman, M., 2021. Proton irradiation in simplified PERC silicon solar cells: A simulation-based framework. ECS Journal of Solid State Science and Technology. 10(5), 055007.

[4] Weiss, C., Park, S., Lefèvre, J., et al., 2020. Electron and proton irradiation effect on the minority carrier lifetime in SiC passivated p-doped Ge wafers for space photovoltaics. Solar Energy Materials and Solar Cells. 209, 110430.

[5] Serge, T.G., Bernard, Z., Bruno, K., et al., 2019. Theoretical study of proton radiation influence on the performance of a polycrystalline silicon solar cell. International Journal of Photoenergy. 1-7.

[6] Gubarev, V.N., Semenov, A.Y., Surma, A.M., et al., 2011. Applying proton irradiation for performance improvement of power semiconductors. Power Electronics Europe. 3, 35-38.

[7] Anfimov, I.M., Kobeleva, S.P., Pylnev, A.V., et al., 2017. On the problem of determining the bulk lifetime by photoconductivity decay on the unpassivated samples of monocrystalline silicon. Russian Microelectronics. 46, 585-590.

[8] Koshelev, O.G., Vasiljev, N.G., 2017. Separate determination of the photoelectric parameters of n^+-p (n)-p^+ silicon structure base region by noncontact method based on measurements of quantum efficiency relationships at two wavelengths. Modern Electronic Materials. 3(3), 127-130.

[9] Sam, R., Zouma, B., Zougmoré, F., et al., 2012. 3D determination of the minority carrier lifetime and the pn junction recombination velocity of a polycrystalline silicon solar cell. IOP Conference Series: Materials Science and Engineering. 29(1), 012018.

[10] Bscheid, C., Engst, C.R., Eisele, I., et al., 2019. Minority carrier lifetime measurements for contactless oxidation process characterization and furnace profiling. Materials. 12(1), 190.

[11] Kozlov, V.A., Kozlovski, V.V., 2001. Doping of semiconductors using radiation defects produced by irradiation with protons and alpha particles. Semiconductors. 35, 735-761.

[12] Agafonov, Y.A., Bogatov, N.M., Grigorian, L.R., et al., 2018. Effect of radiation-induced defects produced by low-energy protons in a heavily doped layer on the characteristics of n^+-p-p^+ Si structures. Journal of Surface Investigation: X-ray, Synchrotron and Neutron Techniques. 12, 499-503.

[13] Bogatov, N.M., Grigorian, L.R., Kovalenko, A.I., et al., 2020. Influence of radiation defects induced by low-energy protons at a temperature of 83 K on the characteristics of silicon photoelectric structures. Semiconductors. 54, 196-200.

[14] Bogatov, N.M., Grigor'yan, L.R., Kovalenko, A.I., et al., 2021. Pulse response characteristics of silicon photovoltaic converters irradiated with low-energy protons. Technical Physics Letters. 47(4), 326-328.

[15] Hu, Z., Hernández, D.M., Martinez, S.N., 2022. Analysis of radiation effects of semiconductor devices based on numerical simulation Fermi-Dirac. Nonlinear Engineering. 11(1), 252-259.

[16] Wen, Y., Zhou, J., 2019. Metamaterial route to direct photoelectric conversion. Materials Today. 23, 37-44.

[17] Vasilevich, U.P., Nguyen, V.Z., Dziatlau, Y.K., 2018. Photoelectric converter for monitoring lighting systems. Doklady BGUIR. (7), 144-148.

[18] Zhu, M., Liu, X., Wang, Y., et al., 2022. Re-

search and design of photoelectric converter for quantum gravimeter. Journal of Physics: Conference Series. 2383(1), 012032.

[19] Bogatov, N., Grigoryan, L., Klenevsky, A., et al., 2020. Modelling of disordering regions in proton-irradiated silicon. Journal of Physics: Conference Series. 1553(1), 012015.

[20] Harutyunyan, V., Sahakyan, A., Manukyan, A., et al., 2023. Introduction rates of electrically active radiation defects in proton irradiated n-type and p-type Si monocrystals. Journal of Electronic Materials. 1-8.

[21] Shockley, W., 1949. The theory of p-n junctions in semiconductors and p-n junction transistors. Bell System Technical Journal. 28(3), 435-489.

[22] Fahrenbruch, A., Bube, R., 2012. Fundamentals of solar cells: Photovoltaic solar energy conversion. Elsevier: Amsterdam.

BILINGUAL PUBLISHING GROUP

Semiconductor Science and Information Devices
https://journals.bilpubgroup.com/index.php/ssid

ARTICLE

Cooperative Relaying in a Three User Downlink NOMA System Using Dynamic Power Allocation

***Mwewa Mabumba*[1], *Simon Tembo*[1], *Lukumba Phiri*[2*]**

[1] *Department of Electrical and Electronics Engineering, University of Zambia, P. O. Box 32379, Lusaka, Zambia*
[2] *Department of Engineering and ICT, School of Engineering, Information Communications University, P.O. Box 30226, Lusaka, Zambia*

ABSTRACT

Non-orthogonal multiple access (NOMA) represents the latest addition to the array of multiple access techniques, enabling simultaneous servicing of multiple users within a singular resource block in terms of time, frequency, and code. A typical NOMA configuration comprises a base station along with proximate and distant users. The proximity users experience more favorable channel conditions in contrast to distant users, resulting in a compromised performance for the latter due to the less favorable channel conditions. When cooperative communication is integrated with NOMA, the overall system performance, including spectral efficiency and capacity, is further elevated. This study introduces a cooperative NOMA setup in the downlink, involving three users, and employs dynamic power allocation (DPA). Within this framework, User 2 acts as a relay, functioning under the decode-and-forward protocol, forwarding signals to both User 1 and User 3. This arrangement aims to bolster the performance of the user positioned farthest from the base station, who is adversely affected by weaker channel conditions. Theoretical and simulation outcomes reveal enhancements within the system's performance.

Keywords: NOMA; Cooperative NOMA; Decode and forward; Dynamic power allocation

1. Introduction

Future wireless communication requires high data rates, low latency, improved accuracy, enhanced quality of service, and more. These demands intro-

*CORRESPONDING AUTHOR:
Lukumba Phiri, Department of Engineering and ICT, School of Engineering, Information Communications University, P.O. Box 30226, Lusaka, Zambia; Email: phirilukumba@gmail.com

ARTICLE INFO
Received: 20 October 2023 | Revised: 15 November 2023 | Accepted: 17 November 2023 | Published Online: 21 November 2023
DOI: https://doi.org/10.30564/ssid.v5i1.6028
CITATION
Mabumba, M., Tembo, S., Phiri, L., 2023. Cooperative Relaying in a Three User Downlink NOMA System Using Dynamic Power Allocation. Semiconductor Science and Information Devices. 5(1): 26-32. DOI: https://doi.org/10.30564/ssid.v5i1.6028

COPYRIGHT
Copyright © 2023 by the author(s). Published by Bilingual Publishing Group. This is an open access article under the Creative Commons Attribution-NonCommercial 4.0 International (CC BY-NC 4.0) License. (https://creativecommons.org/licenses/by-nc/4.0/).

duce challenges due to signal degradation caused by factors like random fades, diffraction, noise, and other performance-reducing phenomena [1]. Addressing these challenges necessitates technological advancements. The emerging 5G technique known as Non-Orthogonal Multiple Access (NOMA) offers superior performance in terms of boosting spectral efficiency compared to conventional multiple access methods. NOMA enables the support of multiple users within a single resource block, thereby enhancing both individual user and overall system throughput [2]. In a typical NOMA setup, users communicate individually with the base station, treating signals from other users as interference. Orthogonal Multiple Access (OMA) frameworks struggle to accommodate high-speed communication applications and a growing user base. Consequently, the shift toward NOMA techniques for 5G is evident, as it outperforms OMA techniques across various parameters, including user fairness, throughput, and data rates [3]. Scientific research confirms that the integration of Non-Orthogonal Multiple Access with recommended wireless technologies yields superior results [4], especially when incorporating features like antenna diversity, massive multiple-input multiple-output architecture, equitable data rates, energy efficiency, cooperative relaying, beamforming and equalization, network coding, and space-time coding [5].

This article primarily focuses on enhancing the performance of distant users within a Non-Orthogonal Multiple Access (NOMA) system by introducing the concept of cooperative relay communication.

The exploration of cooperative relay networks has attracted significant research attention due to its potential to enhance efficiency and system capacity [6]. The fundamental principle of cooperative NOMA involves designating one of the NOMA users as a relay. To elaborate, the transmission process of cooperative NOMA unfolds in two distinct phases or time slots. During the initial phase, the Base Station (BS) disseminates superimposed messages to M NOMA users. In the subsequent phase, a user endowed with strong channel conditions (referred to as the strong user) assumes the role of a relay. This relay user employs Amplify-and-Forward (AF), Decode-and-Forward (DF), or a hybrid AF/DF approach to transmit the deciphered messages to a user possessing weaker channel conditions. This cooperative action enhances the reliability of the weaker user [7].

2. Literature review

Cooperative communications in conjunction with NOMA presents an additional avenue for augmenting user performance. Non-Orthogonal Multiple Access (NOMA) is an auspicious radio access approach for the upcoming generation of wireless networks. Research on NOMA-based cooperative relay networks has been detailed in research by D. Wan, M. Wen, F. Ji et al. [8]. They initiate by introducing current relay-assisted NOMA systems, categorizing them into uplink, downlink, and composite architectures. The principles and key characteristics of these systems are explored, followed by an extensive comparison encompassing aspects like spectral efficiency, energy efficiency, and total transmit power. A new approach termed hybrid power allocation is proposed for the composite architecture. This strategy reduces computational complexity and signaling overhead while incurring a minor sum rate decline.

An innovative concept of Cooperative Communication has been researched to manage challenges like abundant channel access, intricate interference settings, varying networks, and energy-intensive environments. This concept, geared towards high signal coverage and capacity among mobile devices, hinges on resource allocation techniques for robust interference management, resource scheduling, and user matching. Several strategies addressing various technological facets of cooperative communication allocation techniques, including relay nodes, signal forwarding, and transceiver diversity gain, are investigated by W. Guo, N. M. F. Qureshi, I. F. Siddiqui, and D. R. Shin [9].

In a separate study, M. Ajmal and M. Zeeshan [1] introduce a novel hybrid cooperative communication method for multiuser power domain NOMA. This approach leverages amplify-and-forward (AF) and decode-and-forward (DF) techniques through a

strong user acting as a relay for a weak user in a cellular system. This exploits NOMA's inherent feature that a strong user possesses prior knowledge of a weak user with poor channel conditions. Analysis of Bit Error Rate (BER) curves demonstrates that cooperative communication enhances the performance of weak users situated at the cellular system's edge.

Another proposal presents a two-stage superposed transmission for the Cooperative Relay Network (CRN) within a finite time slot framework of the NOMA system by W. Duan et al. [6]. The scheme employs Maximum Ratio Combining (MRC) and Successive Interference Cancellation (SIC) to jointly decode source and relay node receptions across multiple time slots, utilizing a superposition code for the relay node's transmitted signal. The performance of this system is evaluated in terms of ergodic sum rate, outage probability, and outage capacity, substantiated by corresponding closed-form expressions. The scheme's theoretical derivations align well with simulation results, exhibiting notably enhanced transmission rates compared to TDMA and conventional NOMA schemes.

Additionally, a two-stage relay selection strategy for NOMA networks encompassing DF and AF relaying protocols has been introduced in research by Z. Yang, Z. Ding, and P. Fan [10]. The architecture involves a base station communicating with two users through multiple relays. Lastly, a dual-hop cooperative relaying scheme using NOMA has been explored by M. F. Kader, M. B. Shahab, and S. Y. Shin [11]. This system enables two sources to communicate with their corresponding destinations in parallel over the same frequency band, facilitated by a shared relay.

To our best understanding, the majority of investigations into cooperative NOMA have centered around fixed power allocation methodologies, neglecting the dynamic aspect of power allocation that takes the channel's condition into account. Inadequate power allocation could significantly impact the effectiveness of a cooperative network. Therefore, this study delves into the implications of dynamic power allocation on the operational efficiency of cooperative NOMA, particularly focusing on its potential to enhance the system's performance in terms of outage probability and system capacity. The key focal points of this research are as follows:

1) We propose and thoroughly explore the concept of dynamic power allocation within a three-user cooperative NOMA configuration involving a relay that employs the Decode-and-Forward (DF) protocol.

2) To facilitate accurate comparison, we devise a cooperative network integrating reference Orthogonal Multiple Access (NOMA) as a benchmark. The findings demonstrate that the proposed Cooperative NOMA (CNOMA) scheme surpasses the latter approach when perfect Successive Interference Cancellation (SIC) is employed at the relay and at User 3.

3. System model

Figure 1 depicts a simplified scenario of a downlink NOMA system involving three users, namely User 1 (U1), User 2 (U2), and User 3 (U3), along with a solitary base station (BS) situated within a single cell. In this illustration, U2 is designated as the robust user and simultaneously serves as a relay. It is worth noting that in reality we would have several number of users as well as relays and the system model will always differ, but just for the sake of simplicity we decided to use three users with one acting as a relay. In this research, we considered a downlink scenario where the base station communicates with multiple users that power allocation is being performed at the base station and at the relay is essential to optimize the relays amplification and forwarding process. This configuration assumes ideal successive interference cancellation (SIC) receivers and employs Rayleigh fading for all signal links. The diagram showcases the transmission of signals from the BS to U1 and subsequently through an intermediary U2 functioning as a relay. Each node in this setup is outfitted with a sole antenna, while the relay operates in a half-duplex mode utilizing the decode-forward strategy.

The cooperative NOMA paradigm is governed by two distinct phases, namely the transmission phase

(Phase 1) and the cooperative phase (Phase 2) [7].

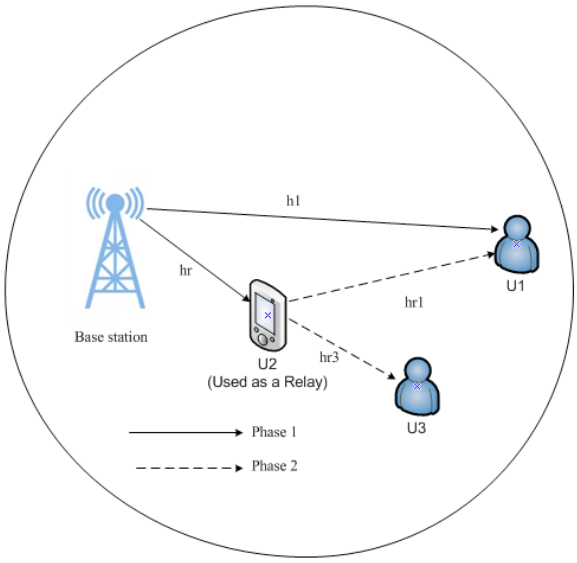

Figure 1. The three-user cooperative NOMA network.

Phase 1

The BS transmits a superposition-coded signal to User 1 and relay, which is generally given by:

$$S_t = \sum_{i=1}^{n} \sqrt{P\alpha_i} x_i \quad (1)$$

where, P = total transmitted power, α_i = power allocation coefficient, and x_i = modulated information of users.

For the cooperative NOMA system under consideration, the transmitted signal for User 1 and User 2 will be written as:

$$\sqrt{P_A\alpha_1}x_1 + \sqrt{P_A\alpha_2}x_2 \quad (2)$$

where, P_A denotes the transmit power of the BS, α_1 and α_2 denote the power allocation coefficients for User 1 and User 2 respectively for the symbol x_1 and x_2.

Assuming that User 1 is the cell edge from the viewpoint of the BS, thus:

$$\alpha_1 > \alpha_1,\ \alpha_1 + \alpha_2 = 1$$

The received signal at U1 and relay during the first phase are given by:

$$R_{BR} = h_{BR}\left(\sqrt{P_A\alpha_1}x_1 + \sqrt{P_A\alpha_2}x_2\right) + n_R \quad (3)$$

$$R_{BU1} = h_{BU1}\left(\sqrt{P_A\alpha_1}x_1 + \sqrt{P_A\alpha_2}x_2\right) + n_{U1}(t_1) \quad (4)$$

where h_{BR} and h_{BU1} are the channel coefficients between BS and relay as well as BS and U1. Whereas $n(.)$ represent the additive white Gaussian noise at the receivers respectively and (t_1) denotes the first phase.

The general expression for the received SNR is given by:

$$\gamma = \frac{signal\ power}{interference + noise}$$

The received SNRs for symbols at the relay are respectively given by:

$$\gamma_{BR}^{X1} = \frac{|h_{BR}|^2\alpha_1 P_A}{|h_{BR}|^2\alpha_1 P_A + \sigma^2} \quad (5)$$

$$\gamma_{BR}^{X2} = \frac{|h_{BR}|^2\alpha_2 P_A}{\sigma^2} \quad (6)$$

On the other hand, U1 treats the symbol x_2 as noise to acquire a symbol x_1 from (4). The received SNR for the symbol x_1 at U1 is given by:

$$\gamma_{BU1}^{X1} = \frac{|h_{BU1}|^2\alpha_1 P_A}{|h_{BU1}|^2\alpha_1 P_A + \sigma^2} \quad (7)$$

Phase 2

In C-NOMA, the relay forwards x_2 to U1 and also transmits its superposed signal given by:

$$\sqrt{P_R\beta_1}x_2 + \sqrt{P_R\beta_2}x_R \quad (8)$$

where, P_R denotes the transmit power of the relay, β_1 and β_2 denotes the power allocation coefficients for the symbol x_2 and x_R. It is assumed that U1 is the far user from the viewpoint of the relay, therefore:

$$\beta_1 > \beta_2,\ \beta_1 + \beta_2 = 1$$

The received signal in the second phase at U1 and U3 are respectively given by:

$$R_{RU1} = h_{RU1}\left(\sqrt{P_R\beta_1}x_2 + \sqrt{P_R\beta_2}x_R\right) + n_{U1}(t_2) \quad (9)$$

$$R_{RU3} = h_{RU3}\left(\sqrt{P_R\beta_1}x_2 + \sqrt{P_R\beta_2}x_R\right) + n_{U3} \quad (10)$$

where h_{RU1} and h_{RU3} are the channel coefficients between R and U1 as well as R and U3. Whereas $n(.)$ represent the additive white Gaussian noise at the receivers denoted users respectively and (t_2) denotes the second phase.

U3 performs SIC by decoding the symbol x_2 and treating symbol x_R as noise, and then cancels it to acquire a symbol $x_R$from (10). The received SNRs for the symbol x_2 and x_R at U3 are respectively given by;

$$\gamma_{RU3}^{X2} = \frac{|h_{RU3}|^2\beta_1 P_R}{|h_{RU3}|^2\beta_2 P_R + \sigma^2} \quad (11)$$

$$\gamma_{RU3}^{XR} = \frac{|h_{RU3}|^2 \beta_2 P_R}{\sigma^2} \quad (12)$$

U1 treats symbol x_R as noise when decoding x_2 from (9). The received SNR for the symbol x_2 at U1 is obtained as:

$$\gamma_{RU1}^{X2} = \frac{|h_{RU1}|^2 \beta_1 P_R}{|h_{RU1}|^2 \beta_2 P_R + \sigma^2} \quad (13)$$

The achievable rates for each symbol are given as follows. For SIC, the relay should decode x_1, and the achievable rate associated with x_1 is obtained from (5) and (7) as:

$$C_{X1} = \frac{1}{2} min\left\{log_2(1+\gamma_{BU1}^{X1}), log_2(1+\gamma_{BR}^{X1})\right\} \quad (14)$$

As the achievable rate of DF relaying is dominated by the weakest link, U3 must decode x_2 for SIC, and the achievable rate related to x_2 is obtained from (6), (13), and (11) as:

$$C_{X2} = \frac{1}{2}\log_2\left\{1 + min\left(\gamma_{BR}^{X2}, \gamma_{RU1}^{X2}, \gamma_{RU3}^{X2}\right)\right\} \quad (15)$$

When U3 succeeds in decoding x_2, the achievable rate associated with x_R *is* given by:

$$C_{XR} = \frac{1}{2}\log_2\left(1 + \gamma_{RU3}^{XR}\right) \quad (16)$$

Performance analysis

This part of the research paper explains ergodic capacity (EC) which is used as a performance metric in wireless communication systems to characterize the average achievable data rate of a communication link over a long period, considering the statistical variations of the channel conditions.

Ergodic capacity (EC)

EC is a concept used in information theory and communication systems to quantify the average data rate that can be reliably transmitted between the transmitter and receiver under varying channel conditions. Ergodic capacity is calculated by taking the average of the capacity achieved over different channel realizations, considering the probability distribution of the channel conditions [12]. For a wireless channel with signal-to-noise ratio (SNR) γ, the ergodic capacity can be expressed mathematically as:

$$C = E[\log_2(1+\gamma)] \quad (17)$$

where, $E[.]$ is the expectation operator and $\log_2(1+\gamma)$ is the instantaneous capacity of the channel for a given SNR (γ).

4. Simulation results

Figure 2 below gives a comparison of the simulation results for the proposed C-NOMA employing decode-forward and existing CNOMA with decode-forward. NOMA's power allocation scheme plays a crucial role in the determination of results. In these results, dynamic power allocation has been considered and it can be seen that the system performance shows an improvement in terms of ergodic system capacity. As the transmit SNR increases, the quality of the received signal improves, which leads to higher capacity which is dependent on the power allocation strategy. At 10dB, the rate gain of proposed CNOMA over existing CNOMA is 10% meanwhile when the SNR is at 30 dB, there's about a 25% increase in rate gain over existing CNOMA.

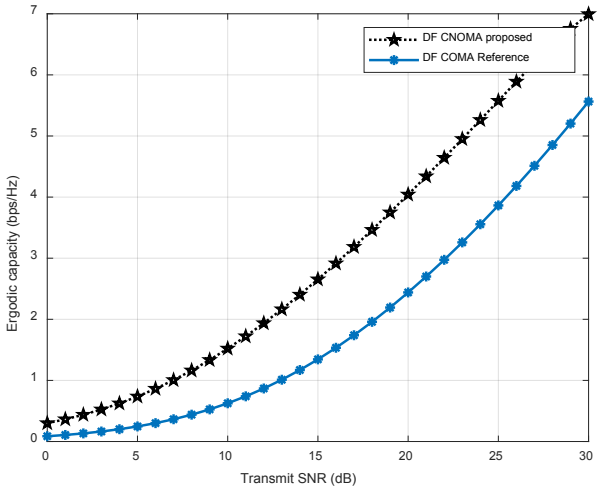

Figure 2. Comparison of DF CNOMA and DF COMA.

5. Conclusions

We introduced a cooperative NOMA framework involving three users, where the user situated closer to the base station serves as a relay using the decode-and-forward relaying protocol. Additionally, we formulated a cooperative OMA setup utilizing the decode-and-forward protocol, serving as a refer-

ence point for comparison. The outcomes of our investigation demonstrate that the decode-and-forward protocol, coupled with dynamic power allocation in NOMA, outperforms the decode-and-forward protocol in OMA. As a next step, our research aims to explore the potential of incorporating a hybrid amplify-and-forward/amplify-and-forward approach in more complex scenarios involving multiple participants. Secondly, since wireless channels are often frequency selective we intend to consider it as well as frequency offset in our research in order to see how the performance will be. Finally, we will analyse the system performance considering bit error rate (BER) vs average signal to noise ratio (SNR) per bit of NOMA and OMA systems.

Author Contributions

Author 1: Came up with the idea of researching on how NOMA would behave when it's incorporated with cooperative relaying using dynamic power allocation with a relay employing decode and forward. The system design was proposed of a three user case scenario.

Author 2: The main contribution was that, he being the main supervisor was responsible to see to it that the research objectives were met and that the system was designed accordingly.

Author 3: Co-supervisor, was responsible for grammatical and spelling corrections. He had to peer review the entire document.

Conflict of Interest

There is no conflict of interest.

References

[1] Ajmal, M., Zeeshan, M. (editors), 2021. A novel hybrid af/df cooperative communication scheme for power domain noma. 2021 IEEE 15th International Symposium on Applied Computational Intelligence and Informatics (SACI); 2021 May 19-21; Timisoara, Romania. New York: IEEE. p. 000055-000060.
DOI: https://doi.org/10.1109/SACI51354.2021.9465621

[2] Mabumba, M., Tembo, S., 2023. Dynamic power allocation as a way of improving the performance of users in Downlink Non-Orthogonal Multiple Access (NOMA) for 5G communications. International Journal of Innovative, Science and Research Technology. 8(5).

[3] Su, W., Sadek, A.K., Ray Liu, K.J., 2008. Cooperative communication protocols in wireless networks: Performance analysis and optimum power allocation. Wireless Personal Communications. 44, 181-217.
DOI: https://doi.org/10.1007/s11277-007-9359-z

[4] Ligwa, M., Balyan, V., 2022. A comprehensive survey of NOMA-based cooperative communication studies for 5G implementation. Expert Clouds and Applications. 619-629.
DOI: https://doi.org/10.1007/978-981-16-2126-0_49

[5] Ghous, M., Hassan, A.K., Abbas, Z.H., et al., 2022. Cooperative power-domain NOMA systems: An overview. Sensors. 22(24), 9652.
DOI: https://doi.org/10.3390/s22249652

[6] Duan, W., Jiang, X.Q., Wen, M., et al., 2018. Two-stage superposed transmission for cooperative NOMA systems. IEEE Access. 6, 3920-3931.
DOI: https://doi.org/10.1109/ACCESS.2017.2789193

[7] Mabumba, M., Tembo, S., Phiri, L., 2023. Performance study of Downlink users in Non-orthogonal Multiple Access (NOMA) for 5G communications. Global Journal of Computer Science Technology (E). 23(1), 1-8.

[8] Wan, D., Wen, M., Ji, F., et al., 2018. Non-orthogonal multiple access for cooperative communications: Challenges, opportunities, and trends. IEEE Wireless Communications. 25(2), 109-117.
DOI: https://doi.org/10.1109/MWC.2018.1700134

[9] Guo, W., Qureshi, N.M.F., Siddiqui, I.F., et al., 2022. Cooperative communication resource allocation strategies for 5G and beyond net-

works: A review of architecture, challenges and opportunities. Journal of King Saud University-Computer and Information Sciences. 34(10), 8054-8078.
DOI: https://doi.org/10.1016/j.jksuci.2022.07.019

[10] Yang, Z., Ding, Z., Wu, Y., et al., 2017. Novel relay selection strategies for cooperative NOMA. IEEE Transactions on Vehicular Technology. 66(11), 10114-10123.
DOI: https://doi.org/10.1109/TVT.2017.2752264

[11] Kader, M.F., Shahab, M.B., Shin, S.Y., 2017. Exploiting non-orthogonal multiple access in cooperative relay sharing. IEEE Communications Letters. 21(5), 1159-1162.
DOI: https://doi.org/10.1109/LCOMM.2017.2653777

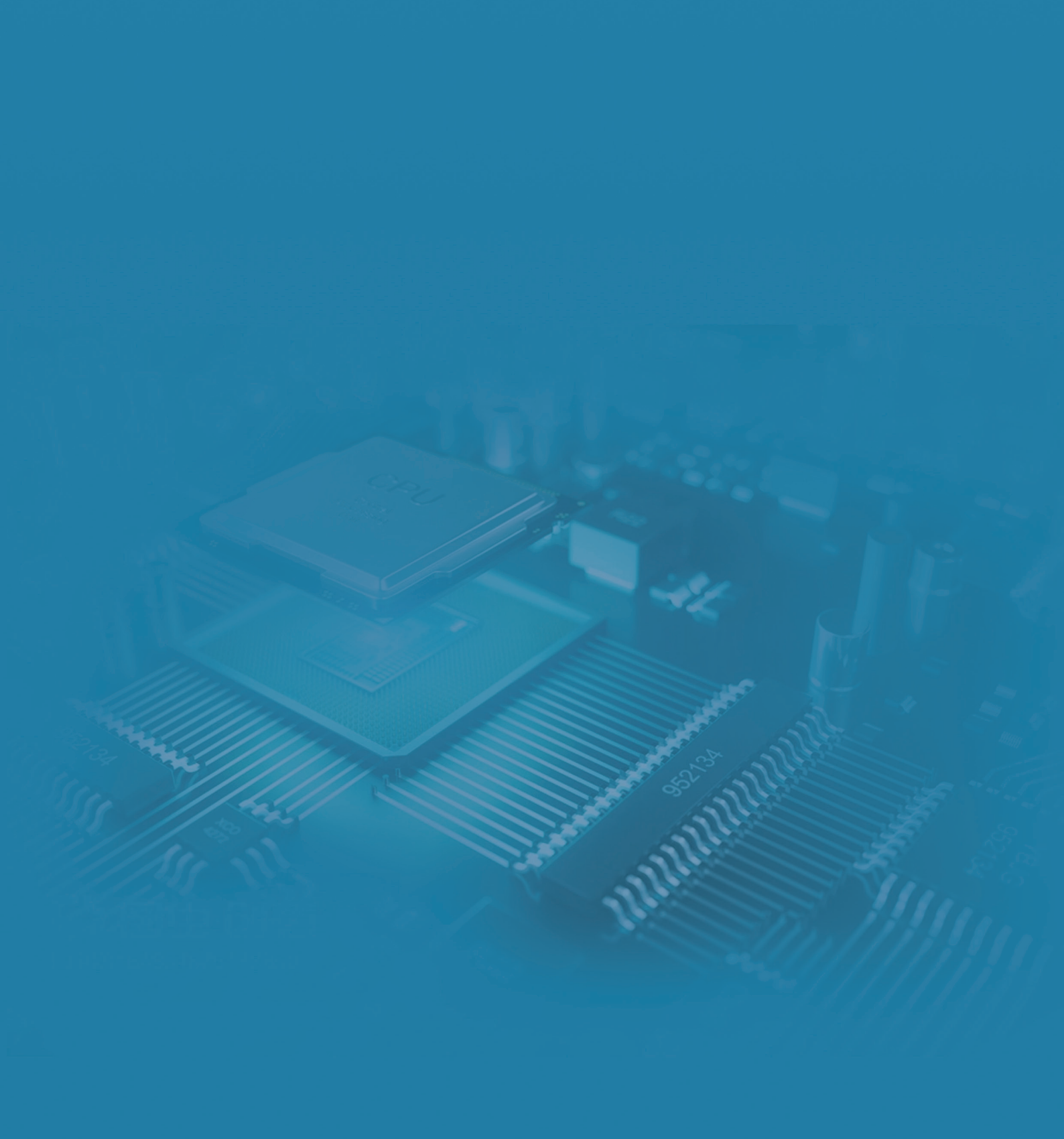

BILINGUAL PUBLISHING GROUP
Tel:+65 65881289
E-mail: contact@bilpublishing.com
Website:https://journals.bilpubgroup.com

2661-3212
01
9 772661 321237